ARTICLES
https://doi.org/10.1038/s41551-020-0584-z

nature biomedical engineering

Check for updates

Gold/alpha-lactalbumin nanoprobes for the imaging and treatment of breast cancer

Jiang Yang[1,2,3], Tai Wang[4], Lina Zhao[5], Vinagolu K. Rajasekhar[6], Suhasini Joshi[4], Chrysafis Andreou[1,2], Suchetan Pal[1,2], Hsiao-ting Hsu[1,2], Hanwen Zhang[1,2], Ivan J. Cohen[1,7], Ruimin Huang[1,2], Ronald C. Hendrickson[8], Matthew M. Miele[8], Wenbo Pei[4], Matthew B. Brendel[9], John H. Healey[6], Gabriela Chiosis[4,10] and Moritz F. Kircher[1,2,11,12,13,14] ✉

Theranostic agents should ideally be renally cleared and biodegradable. Here, we report the synthesis, characterization and theranostic applications of fluorescent ultrasmall gold quantum clusters that are stabilized by the milk metalloprotein alpha-lactalbumin. We synthesized three types of these nanoprobes that together display fluorescence across the visible and near-infrared spectra when excited at a single wavelength through optical colour coding. In live tumour-bearing mice, the near-infrared nanoprobe generates contrast for fluorescence, X-ray computed tomography and magnetic resonance imaging, and exhibits long circulation times, low accumulation in the reticuloendothelial system, sustained tumour retention, insignificant toxicity and renal clearance. An intravenously administrated near-infrared nanoprobe with a large Stokes shift facilitated the detection and image-guided resection of breast tumours in vivo using a smartphone with modified optics. Moreover, the partially unfolded structure of alpha-lactalbumin in the nanoprobe helps with the formation of an anti-cancer lipoprotein complex with oleic acid that triggers the inhibition of the MAPK and PI3K–AKT pathways, immunogenic cell death and the recruitment of infiltrating macrophages. The biodegradability and safety profile of the nanoprobes make them suitable for the systemic detection and localized treatment of cancer.

Surgery represents the primary and, often, the only curative option for most solid cancers. Postsurgical prognosis is directly influenced by whether complete resection has been achieved. At present, there is an unmet clinical need to guide tumour resections with greater precision, enabling complete resection but without the presently used wide-margin resection, which is needed to decrease the rate of tumour recurrences but is often not possible without causing unacceptable morbidity[1]. Wide-margin resections are used because surgeons cannot actually see the true extent of tumours, requiring resection of excessive surrounding normal tissues in case they harbour invisible cancer.

Contemporary nanomedicine holds great promise for improvements in cancer diagnosis and therapeutic drug delivery. Nanoparticles (NPs) without specific targeting moieties can accumulate in molecularly heterogeneous tumours through the enhanced permeability and retention effect[2] (Fig. 1a,b). Sophisticated surface modification and encapsulation with targeting functionalities, drugs and extrinsic imaging probes render NPs versatile theranostic scaffolds, yet simplicity in the rational design of NPs is a key factor for success in clinical translation[3]. Moreover, the clearance of NPs through the urinary system is a highly desirable parameter for minimizing potential toxicity. Noble-metal quantum clusters (QCs)—which comprise fixed finite atoms in an ultrasmall size—occupy an intermediate category between atoms and conventional NPs, exhibiting strong quantum confinements and unique pharmacological and toxicological behaviours. Gold quantum clusters (AuQCs) are promising in biological systems as opposed to semiconductor quantum dots with toxic heavy metals. Gold with its high Z and K-edge ($Z=79$, 80.7 keV) is superior to iodine ($Z=53$, 33.2 keV) in X-ray absorption in both mammography and clinical computed tomography (CT) windows (Fig. 1c). Electron-dense AuQCs with multiple packed Au atoms offer a high local Au concentration and, therefore, possibly a higher contrast[4]. Ultrasmall AuNPs can also have magnetic properties with magnetization peaking at ~3 nm depending on protective ligands[5] and have been used as contrast agents for magnetic resonance imaging (MRI)[6]. Protein-based MRI agents have received considerable attention owing to their improved pharmacokinetics and enhanced relaxivities compared with small-molecule chelators[7]. Protein-bound NPs—such as abraxane, which can be used at higher maximum tolerated doses with fewer adverse events—are effective oncologic therapeutic agents[8]. Furthermore, abraxane resistance occurs by a mechanism that is possibly different from its small-molecule counterpart[9] and was shown to drive macrophage immunostimulatory activation through macropinocytosis[10].

[1]Center for Molecular Imaging and Nanotechnology (CMINT), Memorial Sloan Kettering Cancer Center, New York, NY, USA. [2]Department of Radiology, Memorial Sloan Kettering Cancer Center, New York, NY, USA. [3]State Key Laboratory of Oncology in South China, Collaborative Innovation Center for Cancer Medicine, Sun Yat-sen University Cancer Center, Guangzhou, China. [4]Chemical Biology Program, Sloan Kettering Institute, New York, NY, USA. [5]CAS Key Laboratory for Biomedical Effects of Nanomaterials and Nanosafety, Institute of High Energy Physics, Chinese Academy of Sciences, Beijing, China. [6]Department of Surgery, Memorial Sloan Kettering Cancer Center, New York, NY, USA. [7]Louis V. Gerstner Jr Graduate School of Biomedical Sciences, Memorial Sloan Kettering Cancer Center, New York, NY, USA. [8]Proteomics and Microchemistry Core Laboratory, Memorial Sloan Kettering Cancer Center, New York, NY, USA. [9]Molecular Cytology Core Laboratory, Memorial Sloan Kettering Cancer Center, New York, NY, USA. [10]Breast Cancer Service, Department of Medicine, Memorial Sloan Kettering Cancer Center, New York, NY, USA. [11]Molecular Pharmacology Program, Sloan Kettering Institute, New York, NY, USA. [12]Department of Radiology, Weill Cornell Medical College, New York, NY, USA. [13]Department of Imaging, Dana-Farber Cancer Institute and Harvard Medical School, Boston, MA, USA. [14]Department of Radiology, Brigham & Women's Hospital and Harvard Medical School, Boston, MA, USA. ✉e-mail: moritz_kircher@dfci.harvard.edu

Here we used the globular metalloprotein alpha-lactalbumin (α-LA) for the synthesis of AuQCs, not only because its molecular mass is lower than common carrier proteins, but also because it is the protein component of anti-cancer lipoprotein complexes[11]. Furthermore, it is a naturally occurring dietary protein molecule and is therefore generally regarded as safe by the US Food and Drug Administration. α-LA has high-affinity binding sites for multiple metal ions[12] and shares structural similarities with lysozyme, which is known to bind to Au^{3+} to form NPs[13,14]. We hypothesized that a potential AuQC derived from α-LA could serve as a multimodal imaging probe and could locate tumours depth-independently using CT or MRI and provide high-precision surgical vision in an optimal imaging window by visible excitation and near-infrared (NIR) fluorescence emission aided by a large Stokes shift (Fig. 1d). Amino acids abundant in α-LA—such as tryptophan, lysine and cysteine, which are known to provide nutritional benefits[15]—are also key elements for the synthesis and optical properties of AuQCs. On the basis of the observation that cancer incidence is lower in both breastfeeding mothers and infants, anti-cancer HAMLET, which is the human equivalent of bovine α-LA made lethal to tumour cells (BAMLET), was separated from human milk[11,16,17]. Although α-LA by itself was reported to be an apoptotic switch for lactation suppression and a prophylactic cancer vaccine[18], it is generally considered that its apoptotic effects originate from the partially unfolded state with hydrophobic clusters exposed for complexation with poorly water-soluble unsaturated fatty acids found in food. Human studies of local HAMLET therapy against papillomas and bladder cancer have already been investigated[19,20]. Drug resistance in breast cancer is often associated with mutations in the phosphatidylinositol-3-kinases (PI3K) pathway and simultaneous inhibition of multiple signalling cascades, such as mitogen-activated protein kinases (MAPK)–extracellular regulated protein kinases (ERK) and PI3K–mammalian target of rapamycin (mTOR), is imperative to solve cross-talks[21]. Multikinase inhibitors that function as anti-cancer paradigms by remodelling the kinome, such as lenvatinib, sunitinib and sorafenib, have gained clinical approval. For a combined systemic diagnostic/local therapeutic approach, both whole-body imaging (to locate the tumour) and local imaging abilities with microscopic resolution (to verify drug distribution) are crucial. Here we show that both can be concurrently realized using AuQCs.

Results and discussion

Synthesis and characterization. The source α-LA revealed high purity with a single band near 14 kDa (Supplementary Fig. 1). We used a one-step procedure modulated by α-LA to synthesize ultrasmall AuQCs with fluorescence emissions at 450 nm, 520 nm and 705 nm (termed $AuQC_{450}$, $AuQC_{520}$ and $AuQC_{705}$, respectively) using the same excitation wavelength (Fig. 2a). All AuQCs have <2.5 nm core sizes and <6 nm hydrodynamic sizes (Fig. 2b, Supplementary Fig. 2). α-LA functions not only as a mild reducing reagent but also as a protective molecular ligand, which results in good monodispersity and low zeta potentials that are advantageous for low serum protein binding and long blood circulation[22]. The entire synthesis was precisely controlled by simply varying ligand concentrations, pH and reaction time (Supplementary Figs. 3 and 4). We found that the emission wavelength is correlated with pH and the intensity is dependent on the α-LA concentration (Supplementary Fig. 3f). Time evolution profiles corroborated a short, moderate and long period for $AuQC_{450}$, $AuQC_{705}$ and $AuQC_{520}$, respectively, to reach maximum intensities (Supplementary Fig. 4). AuQCs exhibited good batch-to-batch consistency (Supplementary Fig. 5a–d), acceptable stability in water, phosphate-buffered saline (PBS), cell medium and serum (Supplementary Fig. 5e) and satisfactory photostability (Fig. 2c) without apparent morphological variations (Supplementary Fig. 6). The relative quantum yields (QYs) were determined to be 1.4%, 6.8% and 2.7% for $AuQC_{450}$, $AuQC_{520}$ and $AuQC_{705}$, respectively, with reference to quinine sulfate (Supplementary Fig. 7) and 4.7% for $AuQC_{705}$ with reference to non-sulfonated Cy5.5–*N*-hydroxysuccinimide (NHS; Supplementary Fig. 8). A single-excitation multiplexed example was examined, each associated with an intensity ratio corresponding to a theoretical colour from mixing primary red green blue (RGB; Fig. 2d). Using multispectral unmixing, phantoms of AuQCs in colour codes can be specifically identified at identical excitations (Fig. 2e, Supplementary Fig. 9). On the basis of a gamut of Commission Internationale de l'Éclairage (CIE) 1931 coordinates that is close to standard RGB (Fig. 2f), multiplexed optical coding can be realized by precisely controlled ratios across the entire visible spectrum.

Fluorescence mechanism. AuQCs do not present strong localized surface plasmon resonance, in contrast to 10.6 nm citrate-AuNPs and 2.5 nm tetrakis(hydroxymethyl) phosphonium chloride (THPC)-AuNPs, both of which exhibit localized surface plasmon resonance, high serum protein binding, poor thermally degradability and negligible fluorescence (Supplementary Figs. 10 and 12g). In addition to the minimal interaction with serum proteins, we also found that the specific antibody-binding affinity of α-LA is preserved after synthesis of $AuQC_{705}$ (Supplementary Fig. 11). To elucidate the fluorescence mechanisms of AuQCs through surface ligands, we reduced the disulfide bonds of α-LA and irreversibly blocked the -SH groups with the alkylating agent *N*-ethylmaleimide, as verified using an Ellman's assay (Supplementary Fig. 12a). AuNPs synthesized with thiol-blocked α-LA retained ultrasmall sizes or self-assembled into nanotubes with much weaker fluorescence (Supplementary Fig. 12). We therefore conclude that charge transfers from α-LA ligands to the AuNP core through Au–S bonds are primarily responsible for the fluorescence of AuQCs[23]. This is further supported using gelatin without Cys[24] (Supplementary Fig. 12e–g). By precisely examining the effects of each amino acid in the primary structure of α-LA (Supplementary Fig. 13), it was shown that Trp (high concentrations) and His were associated with $AuQC_{450}$, whereas Trp (low concentrations) and Tyr predominantly determined $AuQC_{520}$. Cys reactivity is strongly associated with protonation states and protein local environment such as pH[25]. Surprisingly, NIR emissions from both Cys and $(Cys)_2$ at high pH were rather weak (Supplementary Fig. 13j,l). At low pH, NIR peaks shifted hypsochromically with 10–100-fold increased intensity (Supplementary Fig. 13i,k), but no NIR peaks were present using α-LA (Supplementary Fig. 3a,b). In fact, α-LA as a complex zwitterionic framework with abundant $-NH_2$ and -COOH groups can modulate local pH and local amino acid concentrations in the microenvironment and therefore tune the effects of amino acids. Many aforementioned reactive amino acids are not solvent-accessible in the native state (Supplementary Fig. 13c–e). Combined mild thermal and pH conditions are therefore necessary to expose these amino acids for the synthesis of AuQCs by disrupting non-covalent interactions and overcoming intramolecular and intermolecular barriers of disulfide bonds that restrict molecular expansion into partially unfolded states. Meanwhile, the solvent-exposed Met90 residue might also induce NIR emissions. All of these results imply that modulation of AuQC fluorescence depends not only on the primary structure of α-LA, but also on secondary and tertiary structures and conformational changes. Far-ultraviolet circular dichroism (CD) spectra demonstrated that the secondary structures of α-helices decreased slightly in $AuQC_{450}$ but substantially in $AuQC_{520}$ and $AuQC_{705}$ with minimal renaturation, whereas β-sheets and flexible random coils increased in all AuQCs with largely unaltered β-turns (Fig. 2g), indicating partial retention of rigid and stable secondary conformation. Near-ultraviolet CD spectra indicated nearly a complete

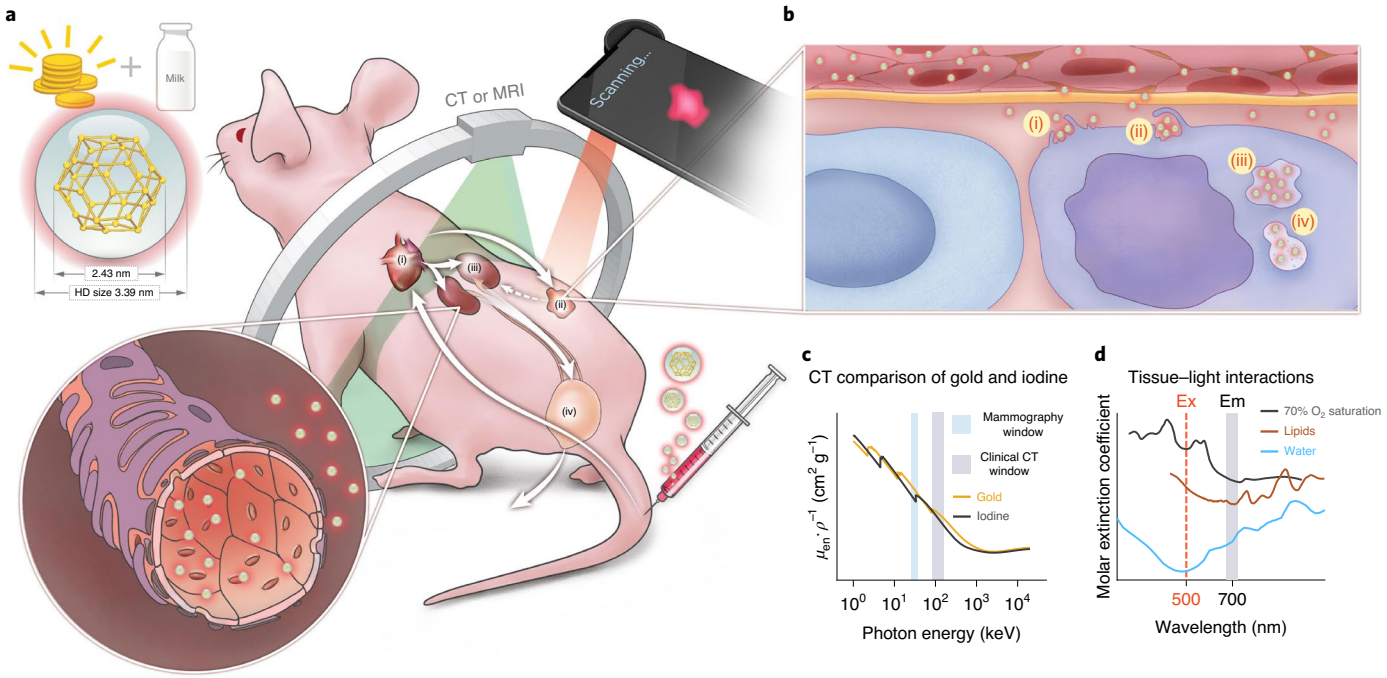

Fig. 1 | Concept of renally clearable AuQC$_{705}$ for cancer imaging. a, Schematic of the NIR fluorescent AuQC$_{705}$ nanoprobe in ultrasmall size synthesized from gold precursors and milk protein α-LA intravenously injected through the tail vein of a mouse bearing a human breast tumour. AuQC$_{705}$ circulates into the cardiac blood pool (i) and passively targets the tumour (ii) through its highly permeable angiogenic vasculatures for imaging. The high specificity of passive tumour targeting and retention results from the combined effects of malformed leaky tumour vasculatures and poor extravasation of impaired lymphatic vessels, which are both absent in healthy tissues. Excessive AuQC$_{705}$ is cleared from the bloodstream by glomerular filtration of renal tubules (iii) and urinary excretion of the bladder (iv). HD, hydrodynamic size. **b**, In the well-organized α-LA framework that dictates its biological identity and governs molecular pathways, AuQC$_{705}$ permeates the tumour via fenestrations in arterioles and capillaries while barely penetrating normal blood vessels which lack such fenestrations. Endocytosis of AuQC$_{705}$ is mediated by macropinocytosis of cancer cells, which sustains survival and proliferation using extracellular proteins as nutrient pathways in a series of steps, including cytoskeleton rearrangement and membrane ruffling (i); ruffle fold-back and engulfment (ii); irregularly shaped large macropinosome vesicle trafficking (iii); and lysosomal catabolism (iv). **c**, Gold with high *Z* and high *K*-edge absorption (orange line) provides superior CT contrast compared with clinically approved iodine (black line) in mammography and clinical CT windows. Data were retrieved from the National Institute of Standards and Technology. $\mu_{en}\ \rho^{-1}$, mass energy-absorption coefficient. **d**, Absorption spectra of major endogenous chromophores in breast tissues, assuming an artery–vein distribution of 70% tissue oxygen saturation[94]. The optical imaging window of AuQC$_{705}$ is optimal, with an excitation (Ex) wavelength of 500 nm in the visible region and an emission (Em) wavelength of 700 nm in the NIR region in which HbO_2–Hb, lipids and water have low absorption, together with a large Stokes shift that substantially reduces autofluorescence.

loss of tertiary structures in AuQC$_{520}$ and AuQC$_{705}$ and a partial loss in AuQC$_{450}$ (Supplementary Fig. 14a). Partial unfolding was also confirmed by bathochromic shift of intrinsic Trp fluorescence (Supplementary Fig. 14b). Unordered protein structures enable the adjustment of favourable orientation for cellular binding and translocation[26] and are the prerequisite for forming antitumour lipoprotein complexes[27]. In general, Au^{3+} was coordinated with amino acids of α-LA, such as His, Asp and Glu, and reduced to Au^+ to form Au^+/α-LA complexes. Controlled assembly of Au^+ induced by aurophilic interactions aggregated as nucleation centres[28] and entrapped clustered Au^+ was further progressively reduced in situ into metallic Au in the α-LA framework, cooperatively mediated by pH and α-LA ligand concentrations. The number of atoms in AuQCs in the internal space of α-LA was controlled by conformational changes and reduction abilities. Emissions at 450 nm, 520 nm and 705 nm are primarily attributed to Au_{3-7}, Au_{11} and $Au_{32/38}$ at atomic scale, respectively, by matrix-assisted laser desorption/ionization time-of-flight mass spectrometry (MALDI–TOF-MS; Supplementary Fig. 15). AuQCs can be efficiently taken up by cancer cells in vitro (Supplementary Fig. 16) and spectrally differentiated in mice (Fig. 2h). AuQC$_{705}$ has a superior in vivo imaging signal-to-noise ratio and was therefore selected as the molecular imaging probe in the rest of our study.

Macropinocytosis for intracellular trafficking. Efficient cellular uptake is the premise for cancer molecular imaging and therapy. Ultrasmall 2 nm AuNPs bearing identical surface ligands have shown increased uptake and penetration compared with 6 nm and 15 nm counterparts[29]. Macropinocytosis is a highly conserved Ras-driven and dynamin-independent primary endocytotic pathway for engulfing extracellular and membrane-bound substances in large (>0.2 μm) heterogeneous vesicles that are known as macropinosomes[30]. Protein macropinocytosis is an essential amino acid source for mTOR-complex-1-activated cancer cells derived from lysosomal proteolytic degradation to support proliferation in vitro and in vivo[31]. Treatment of selective pharmacological modulators—including Na^+/H^+ exchange inhibitor 5-(*N*-ethyl-*N*-isopropyl)-amiloride (EIPA), actin function and polymerization inhibitor cytochalasin D, and the PI3K inhibitors NVP-BEZ235 and wortmannin—effectively blocked endocytosis of AuQC$_{705}$ in the human breast cancer cell line MDA-MB-231 (Fig. 3a,b), demonstrating actin-driven PI3K-depedent macropinocytosis. Owing to low Ras-GTPase activity and inactivated Ras, BxPC-3 cells are insensitive to the macropinocytosis inhibitor EIPA[32], whereas MDA-MB-231 cells carry mutated KRAS that is responsible for strong macropinocytosis[33] (Supplementary Fig. 17). We next evaluated the uptake specificity of AuQC$_{705}$ in MDA-MB-231 cells, which exhibited a dose-dependent

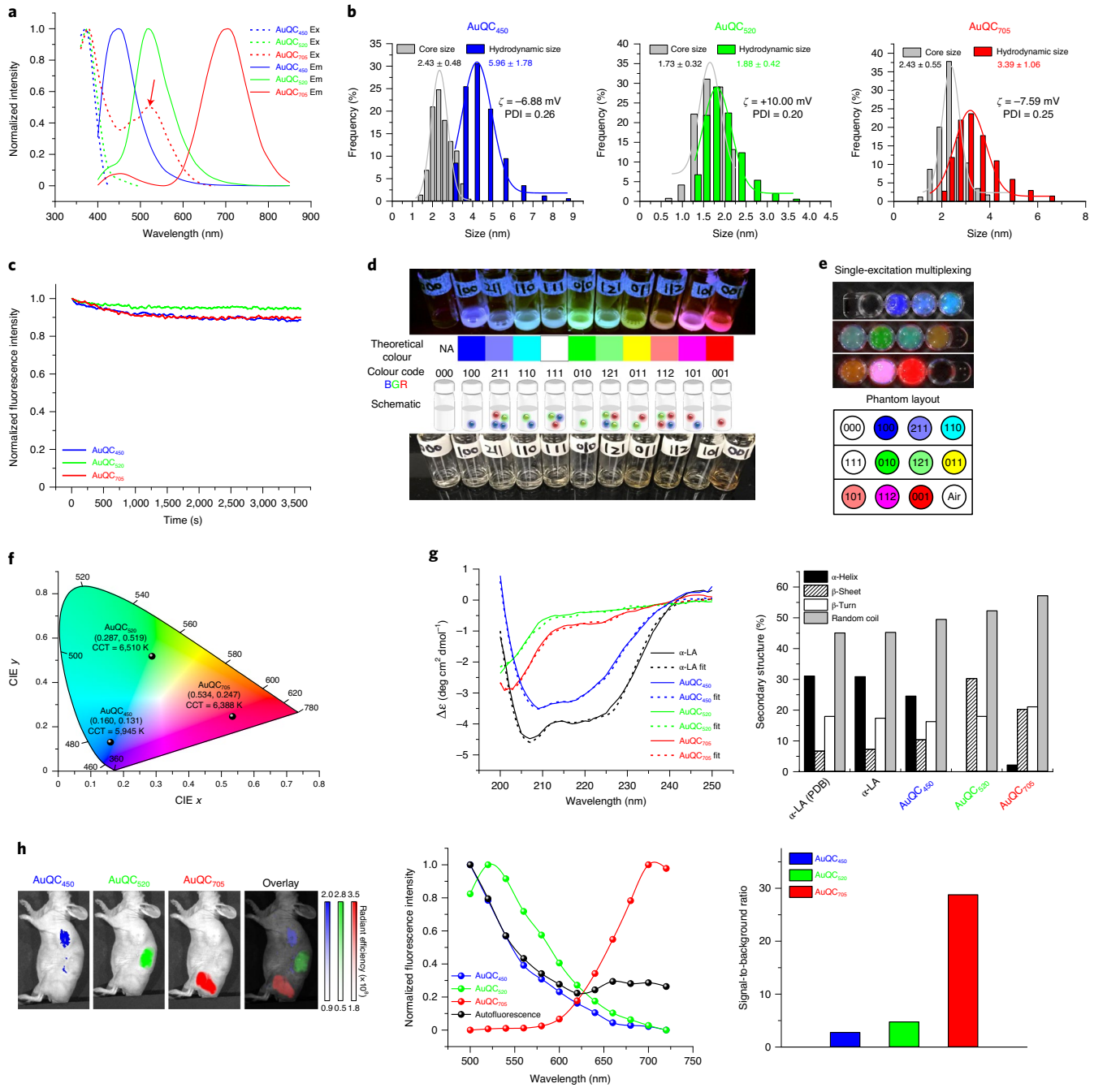

Fig. 2 | Characterization of AuQCs. a, Excitation (dotted lines) and emission (solid lines; excitation, 360 nm) spectra of AuQCs demonstrating maximum excitation peaks at 370–380 nm and emission peaks at 450 nm, 520 nm and 705 nm. A secondary excitation at 520 nm for $AuQC_{705}$ was identified (arrow). **b**, The size distribution of AuQCs, showing core sizes measured using TEM and hydrodynamic diameters measured using dynamic light scattering in PBS. Zeta potentials and polydispersity index (PDI) are indicated. **c**, The photostability of AuQCs at 360 nm continuous exposure. **d**, Single-excitation optical colour coding by AuQCs. The photographs were taken under 302 nm ultraviolet excitation (top) and white light (bottom). Multiplexed intensities can realize theoretically mixed RGB colours. 000, deionized water without AuQCs. NA, not applicable. **e**, In vitro single-excitation multiplexed fluorescence imaging. Images were multispectrally unmixed with spectra of AuQCs and coded in RGB pseudocolours. **f**, CIE 1931 *xy* chromaticity diagram showing the coordinates and correlated colour temperatures (CCT) of AuQCs with a large gamut. **g**, Far-ultraviolet CD spectra of AuQCs and native α-LA. Secondary-structure compositions were determined using BeStSel. Apo-state bovine α-LA acquired from RSCB (Protein Data Bank, 1F6R) was quantified and matched the experimental data well. Δε, molar circular dichroism. **h**, In vivo single-excitation multiplexing using AuQCs in a J:NU mouse after subcutaneous injection. The unit of radiant efficiency is photons s^{-1} cm^{-2} sr^{-1} $(\mu W\ cm^{-2})^{-1}$. Specific in vivo spectra of AuQCs can be unmixed from tissue autofluorescence and are close to in vitro spectra (Supplementary Fig. 9b). The ratios of averaged specific fluorescence to background were calculated and compared. Excitation wavelength, 430 nm.

behaviour—a typical feature of macropinocytosis[34]—and could not be blocked by excessive competitive α-LA (Fig. 3c). $AuQC_{705}$ showed high degrees of sporadic puncta-like colocalization with the well-established macropinocytosis marker fluorescein isothiocyanate (FITC)–dextran (Fig. 3d, Supplementary Fig. 18). Irregularly shaped large macropinosomes in close proximity to membranes

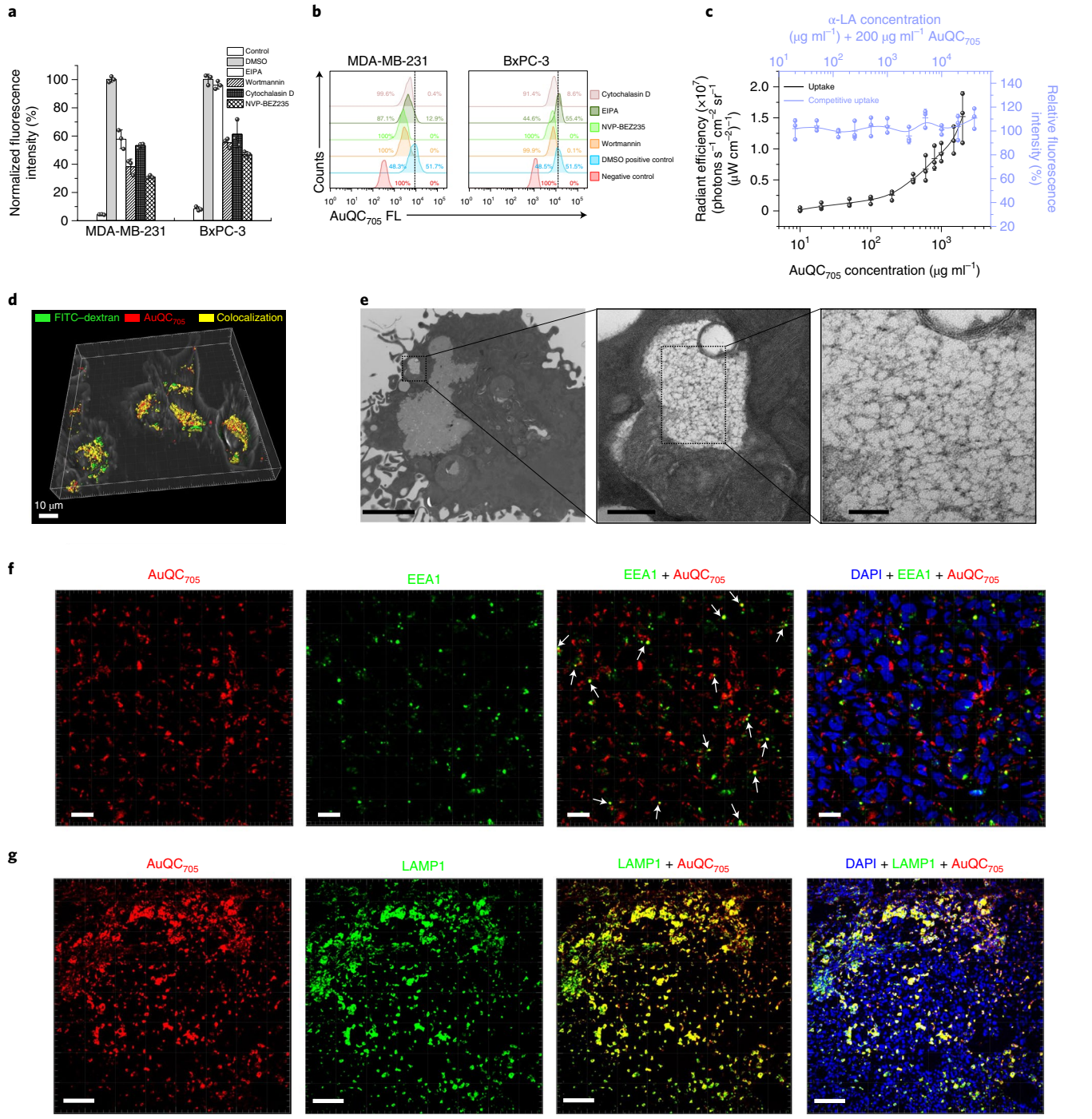

Fig. 3 | The predominant endocytic trafficking pathway of $AuQC_{705}$ in MDA-MB-231 human breast cancer cells and tumours is macropinocytosis. **a**, The effects of pharmacological inhibitors; $n = 3$ biologically independent samples. **b**, Flow cytometry analysis corresponding to **a** with typical single-parameter gating for approximately 50% of the positive control without inhibitors shows inhibition of internalization. **c**, Direct and competitive uptake assays of $AuQC_{705}$ in MDA-MB-231 cells demonstrated typical features of macropinocytosis; $n = 3$ biologically independent samples. While increasing concentrations of $AuQC_{705}$ led to increased uptakes, no obvious blocking effects were observed in the presence of competitive α-LA. **d**, A three-dimensionally (3D) rendered image of a confocal *z* stack of MDA-MB-231 cells overlaid with a bright-field image. $AuQC_{705}$ (red) and the macropinocytosis marker FITC-dextran (green) showed a high degree of cytosolic colocalization (yellow) at 2 h. Scale bar, 10 μm. A complete time course for organelle trafficking is shown in Supplementary Fig. 18. **e**, Ultrastructure analysis with TEM showing an early-formed multivesicular non-homogeneously large-sized (>0.2 μm) and irregularly shaped macropinosome vesicle in MDA-MB-231 cells after 1 h uptake. The cargo is close to the plasma membrane, indicating membrane closure and separation. $AuQC_{705}$ maintained in ultrasmall size can be clearly observed as black dots in the vesicle without apparent aggregation, thereby preserving fluorescence. Scale bars, 2 μm (left), 200 nm (middle) and 50 nm (right). **f**, Immunofluorescence images of MDA-MB-231 tumours from a J:NU mouse 1 h after injection of $AuQC_{705}$; DAPI was used to visualize nuclei (blue). The organelle trafficking of $AuQC_{705}$ (red) and intracellular early endosome–macropinosome marker EEA1 (green) were in punctate patterns. Colocalizations are indicated by white arrows. Scale bars, 20 μm. **g**, The majority of $AuQC_{705}$ (red) was found to end up in late endosomes and lysosomes in tumours 2 h after injection, as observed from the extensive colocalization (yellow) with LAMP1 (green). Scale bars, 100 μm.

with trapped $AuQC_{705}$ were observed in the ultrastructures (Fig. 3e). Internalized $AuQC_{705}$ ended up in the lysosomes in ultrasmall size (Supplementary Fig. 19). In vivo accumulation of $AuQC_{705}$ in breast tumours shared a partially colocalized punctate pattern in the cytoplasm with early endosome antigen 1 (EEA1; Fig. 3f), which is expressed in a proportion of macropinosomes and recruited for maturation[35]. Tumour enrichment of $AuQC_{705}$ involves the dual processes of delivery into extracellular tumour interstitium through tumour-feeding vessels and intracellular macropinocytotic trafficking from extracellular matrices. As a consequence, $AuQC_{705}$ was found in late endosomes and lysosomes, as shown by colocalization with lysosomal-associated membrane protein 1 (LAMP1; Fig. 3g).

$AuQC_{705}$ as a multimodal contrast agent for imaging breast cancer. Ultrasmall $AuQC_{705}$ has a highly monodisperse globular morphology (Supplementary Fig. 20). Photoluminescence excitation of $AuQC_{705}$ presented a NIR emission centred at near 700 nm, independent of excitation wavelength (Supplementary Fig. 21). Besides the primary short-wavelength excitation, a secondary excitation was found in the visible region. The combination of 500 nm excitation and 700 nm emission provides a large Stokes shift that minimizes autofluorescence (Supplementary Fig. 22) and defines an optimal visible–NIR imaging window in which the tissue–light interaction is minimal in the short-wavelength visible and NIR regions (Fig. 1d). NIR fluorescence decreased more substantially at 430 nm excitation with increasing phantom thickness (Supplementary Fig. 23a,b). Similar trends were observed in breast tissues with optimal spatial resolution at 500 nm (Supplementary Fig. 23c–e). $AuQC_{705}$ also displayed CT and MRI contrast that was linearly correlated with concentration (Supplementary Fig. 24). The multi-modality was also verified in cancer cell phantoms (Fig. 4a, Supplementary Figs. 25 and 26). After tail-vein injection into xenograft mice bearing MDA-MB-231 tumours, the tumour can be readily delineated 30 min after injection, owing to rapid perfusion and fast contrast enhancement (Fig. 4b). The tumour remained distinguishable for up to 168 h. Tumour-targeting kinetics of $AuQC_{705}$ peaked at 1 h and gradually decayed through a two-compartment model with a longer tumour retention half-life of 92.6 ± 33.2 h compared with 23.1 ± 9.3 h in normal tissues (Fig. 4c). The prolonged tumour retention potentially reduces the need for readministration and enables multiple examinations through a single injection. Meanwhile, we used a hydrophilic small-molecule NIR dye sulfo-Cy5.5 with similar emission and synthesized its deoxyglucose analogue (2DG) for cancer glycolytic metabolism[36] as well as sulfo-Cy5.5/α-LA protein–dye complex (Supplementary Fig. 27a,b). Tumours could barely be defined by sulfo-Cy5.5 and sulfo-Cy5.5-2DG at early time points with concurrent high uptakes on contralateral sides. By contrast, sulfo-Cy5.5/α-LA has excellent tumour delineation from 30 min as well as a tumour retention half-life close to sulfo-Cy5.5-2DG of which the uptake is facilitated by glucose transporters[37] (Supplementary Fig. 27c–f). α-LA is therefore a promising carrier for cancer imaging. We next conducted non-invasive μCT imaging, which showed pronounced X-ray attenuation in the tumour, kidneys and bladder (Fig. 4d, Supplementary Fig. 28a,b). Interestingly, tumour boundaries that were rich in neovascular vessels were clearly outlined with high accumulations in the periphery, presumably due to a strong enhanced permeability and retention effect. Differential macroscopic distribution of $AuQC_{705}$ was observed from CT with low uptakes in interior necrotic/semi-necrotic hypoxic regions that correlated well with fluorescence (Fig. 4d). Two-dimensional (2D) MRI maps demonstrated shortened longitudinal (T_1) and transverse (T_2) relaxation times after injection (Fig. 4e, Supplementary Fig. 28c). Combining these complementary modalities, $AuQC_{705}$ potentially has the ability to offer both presurgical planning with high spatial resolution and intraoperative guidance with high sensitivity and temporal resolution. We next conducted a NIR-fluorescence-guided stepwise tumour resection near the mammary fat pads and correlated them with intraoperative white-light images (Fig. 4f). We found good congruency between $AuQC_{705}$-illuminated residual tumour and white-light inspection, until complete removal was achieved without any remaining fluorescence in the resection bed. To test its suitability under surgical scenarios at point-of-care settings, we engineered a smartphone device with optics that enables intraoperative guidance (Fig. 4g) and real-time detection of $AuQC_{705}$ enriched in breast tumours (Fig. 4h). Furthermore, $AuQC_{705}$ can also be used for imaging and intraoperative surgical guidance in the murine breast cancer model 4T1 with activated RAS signalling (Supplementary Fig. 29).

Rather than representing one consistent type of neoplasia, breast cancer is deemed to be a diverse set of heterogeneous diseases[38]. Xenograft models derived from human cancer cell lines cannot accurately recapitulate human breast cancers, as the cell lines lack histopathological characteristics and microenvironmental heterogeneity of tumours, as well as the genomic diversity. Patient-derived xenograft (PDX) models created by grafting pieces of human solid tumours into mice are superior in predicting human tumours and minimizing discrepancies between preclinical and clinical outcomes. Bone metastasis is the most frequent metastatic site (>70%) in breast cancer[39]. We established orthotopic breast cancer PDX models by implanting surgically resected fresh tumour tissues of patients with breast cancer bone metastases into the third thoracic mammary fat pad of NSG and J:NU mice for imaging (Fig. 5a). As expected, the histological appearance of PDX tumours is distinct from tumours derived from human breast cancer cell lines, demonstrating regions of angiogenic hypervascularity, abundant extracellular matrix and heterogeneous cell populations (Fig. 5b). $AuQC_{705}$ can efficiently accumulate in triple-negative and hormonal-therapy-resistant oestrogen-receptor-positive PDX tumours (Fig. 5c). Tumour targeting of $AuQC_{705}$ through combined enhanced permeability and retention effect and macropinocytosis, without requiring a specific biomarker, can be a distinct advantage.

Toxicity, pharmacokinetics, clearance and biodistribution. Besides the biocompatibility of gold, protein cloaking to mediate direct contact with biological systems can further mitigate cellular cytotoxicity caused by nanomaterials[40]. In vitro cytotoxicity was evaluated as a function of increasing concentration of $AuQC_{705}$ and no significant difference in cell viabilities was found up to 750 μg ml^{-1} in MDA-MB-231 cells (Supplementary Fig. 30a). BxPC-3 cells with low macropinocytosis were also more resistant to toxicity under high concentrations. The body weight of BALB/cJ wild-type mice did not demonstrate a significant change over time after injection (Supplementary Fig. 30b). There was also no apparent tissue damage in major organs as assessed by histological analysis (Supplementary Fig. 30c). $AuQC_{705}$ complied with classic two-compartment pharmacokinetics (Fig. 5d), with an elimination half-life $t_{1/2\beta} = 6.8 \pm 0.5$ h that results in much longer blood circulation than clinically approved NIR dye indocyanine green ($t_{1/2\beta} = 3.05 \pm 0.89$ min)[41]. The correspondingly large area under the curve of 91.0 %ID h g^{-1} for $AuQC_{705}$ in blood over 48 h after injection leads to the high tumour-targeting efficiency. Major organs collected from BALB/cJ wild-type mice showed a dominant distribution of $AuQC_{705}$ in the urinary system with the majority excreted through the urine (Supplementary Fig. 31). By contrast, sulfo-Cy5.5-conjugated α-LA has an appreciable uptake in the liver and lungs, presumably due to its native rigid structure and oligomerization, although most of it is still excreted into urine. $AuQC_{705}$ in α-LA scaffold is zwitterionic in nature and is well below the molecular mass and hydrodynamic diameter cut-offs for renal clearance[42,43]. Excretion kinetics over 48 h showed that more than 73.1 %ID was effectively excreted into urine (Fig. 5e). Renally cleared $AuQC_{705}$ retained its ultrasmall

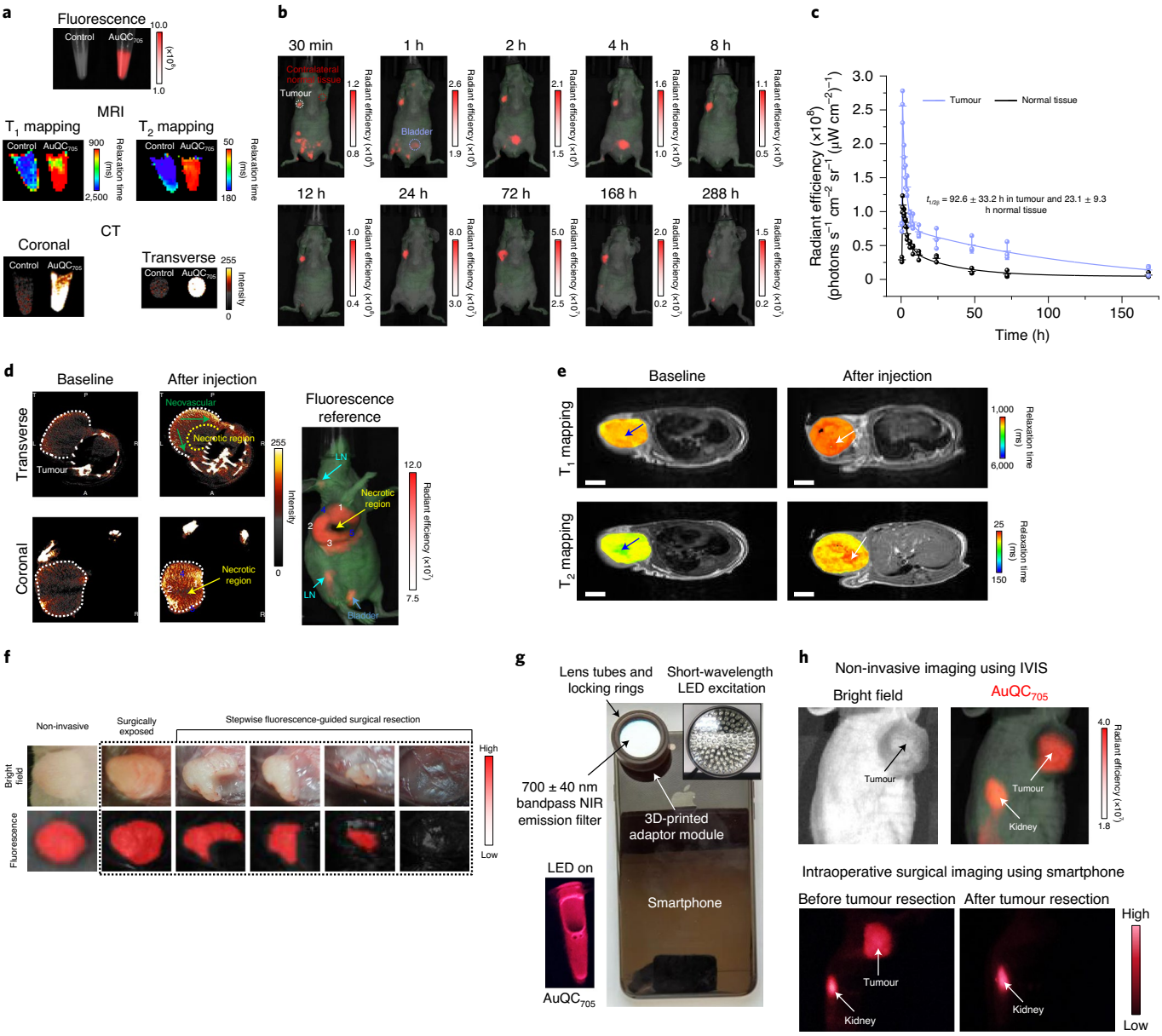

Fig. 4 | AuQC$_{705}$ for imaging breast cancer cells and tumours in living mice. a, Imaging phantoms of pelleted MDA-MB-231 cells by fluorescence, T_1 and T_2 MRI mapping and CT. **b**, Non-invasive in vivo fluorescence imaging of J:NU mice bearing an MDA-MB-231 human breast cancer xenograft after injection of AuQC$_{705}$. The renal clearance of the bladder (blue circle) and the long retention time in the tumour (white circle) are highlighted. AuQC$_{705}$ and autofluorescence are shown in red and green, respectively, and superimposed onto white-light images. **c**, Accumulation and retention kinetics of AuQC$_{705}$ in MDA-MB-231 tumours and normal tissues; $n = 3$ biologically independent animals. **d**, Coronal and transverse planar CT images of an MDA-MB-231 tumour after injection of AuQC$_{705}$. The tumour boundaries are indicated by dotted white lines. Neovascular structures (dark green arrows) in transverse slices show relatively high uptakes. Partitioned tumour subregions 1–3 and 4–5 exhibited high and low local uptakes, respectively, in both modalities. **e**, 2D transverse T_1 and T_2 maps of an MDA-MB-231 tumour superimposed onto anatomical MRI images after injection of AuQC$_{705}$. A high-contrast focal point (white arrows) coinciding with the location of the injection can be clearly observed inside the tumours, whereas the baseline tumours bear a low-contrast necrotic interior site (blue arrows). Scale bars, 5 mm. **f**, NIR-fluorescence-guided intraoperative surgery using AuQC$_{705}$ for a J:NU mouse bearing an MDA-MB-231 breast tumour 24 h after injection. The tumour near the mammary fat pads was surgically exposed and quarters of it were sequentially removed until the entire tumour was completely removed, on the basis of visual inspection and absence of AuQC$_{705}$ signals on the resection bed. **g**, A portable smartphone imaging system prototype. A solution of AuQC$_{705}$ with LED excitation is shown. **h**, Smartphone intraoperative surgical imaging of a J:NU mouse bearing MDA-MB-231 tumours. Skin was removed to mimic a surgical scenario. Images were taken 24 h after injection. Both the tumour and kidney can be clearly outlined and correspond well to the reference non-invasive image. The unit of radiant efficiency in all of the fluorescence images is photons $s^{-1}\,cm^{-2}\,sr^{-1}\,(\mu W\,cm^{-2})^{-1}$.

size in collected urine with no significant difference compared with before the injection (Fig. 5f). The collected urine also retained bright NIR fluorescence (Fig. 5g). Ex vivo fluorescence images confirmed high accumulation and retention primarily in the tumour and kidneys (Fig. 5h–j). AuQC$_{705}$ showed some variations in vitro in artificial lysosomal fluid, but the $Au^{1+/3+}$ may remain coordinated in the α-LA framework as during synthesis (Supplementary Fig. 32). Long-term in vivo retention was shown to be minimal on the basis of silver staining and inductively coupled plasma-mass spectrometry (ICP-MS) analysis (Supplementary Figs. 33 and 34). We also

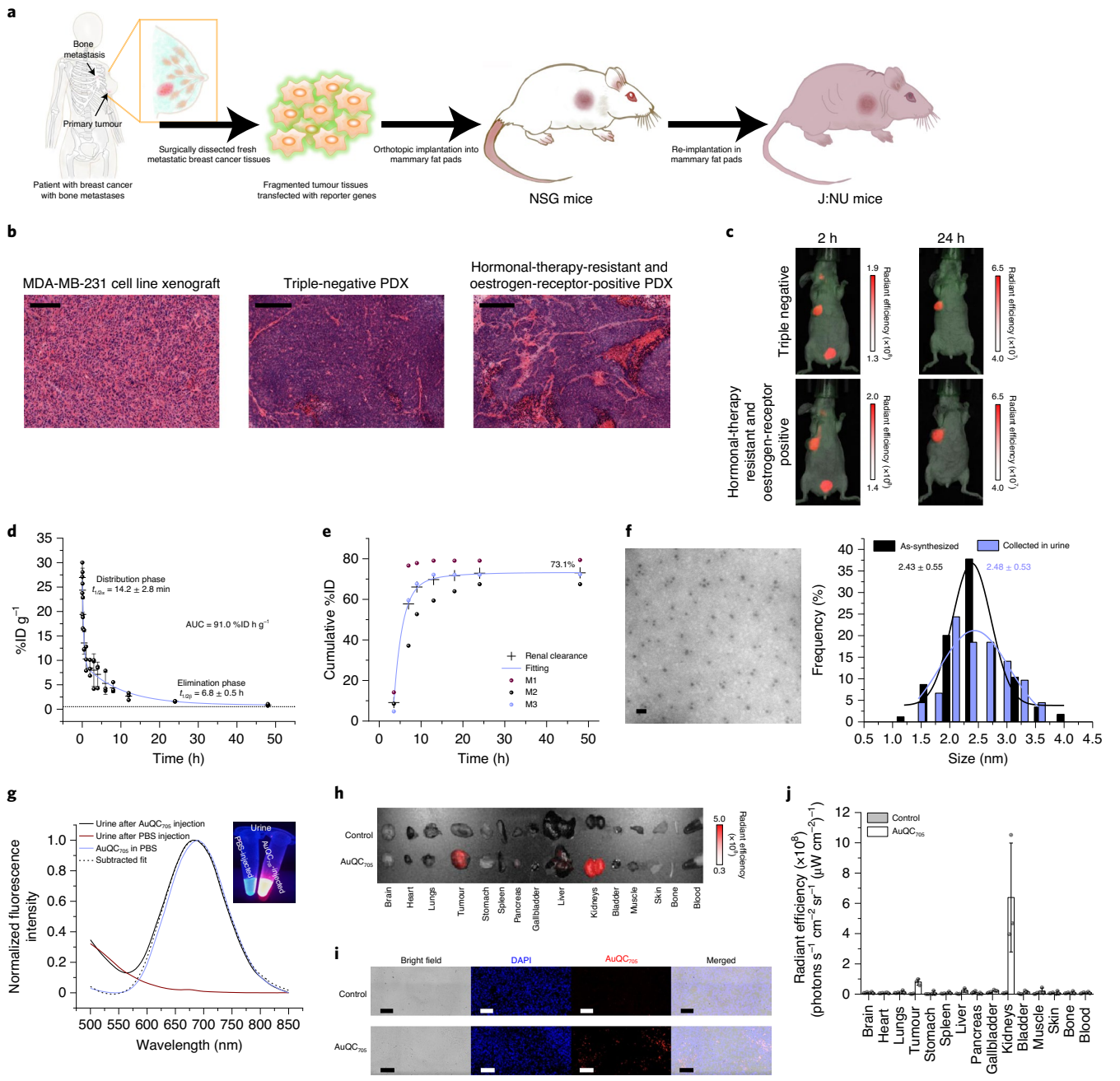

Fig. 5 | PDX model imaging, pharmacokinetics, renal clearance and biodistribution of $AuQC_{705}$. **a**, Schematic of the process to generate orthotopic breast cancer PDX mouse models. **b**, Histology of an MDA-MB-231 tumour and PDX tumours from patients. The human cell-line-derived tumour shows a homogeneous histology. The human PDX tumours reserve the heterogeneity and fidelity of human tumours well, including the microenvironment, rich stroma and abnormal hypervasculatures. Scale bars, 200 μm. **c**, Non-invasive NIR fluorescence imaging of clinically relevant heterogeneous breast cancer PDX models. **d**, The pharmacokinetic profile of $AuQC_{705}$ in BALB/cJ wild-type mice from 0–48 h after injection. Data were fitted by a biexponential function with $R^2 = 0.991$; $n = 3$ biologically independent animals. The dotted line indicates blood signals from control mice injected with PBS. **e**, Cumulative urine excretion profile of $AuQC_{705}$ in BALB/cJ mice in metabolic cages; $n = 3$ biologically independent animals. **f**, TEM image and size distribution of $AuQC_{705}$ collected from excreted urine after injection compared to as-synthesized. Scale bar, 10 nm. Statistical analysis of the sizes was performed using a Student's *t*-test; $P = 0.41$. **g**, Fluorescence spectra of excreted urine from BALB/cJ mice injected with $AuQC_{705}$ and PBS. **h**, Ex vivo fluorescence imaging of organs from J:NU mice bearing MDA-MB-231 tumours. Organs of interest were collected 12 h after injection of $AuQC_{705}$. **i**, Confocal microscopy images of MDA-MB-231 tumour sections with or without injection of $AuQC_{705}$. Scale bars, 100 μm. **j**, Corresponding biodistribution quantified by ex vivo fluorescence imaging 12 h after injection of $AuQC_{705}$; $n = 3$ biologically independent animals. The unit of radiant efficiency in all fluorescence images is photons $s^{-1} cm^{-2} sr^{-1} (\mu W\ cm^{-2})^{-1}$.

performed a long-term panel screening of clinical chemistry and complete blood count; all of the indicators fell within the normal ranges (Supplementary Figs. 35 and 36).

Characterization of $AuQC_{705}$–BAMLET lipoprotein nanocomplex. We next investigated the theranostic potential of $AuQC_{705}$. Human α-LA is the protein constituent of HAMLET, which

specifically kills a broad category of cancer cells from different origins while sparing differentiated mature cells[11]. Preconditioned ion-exchange chromatography and hydrothermal approaches were used by interacting α-LA and unsaturated C18:1 oleic acid (OA)[11,44]. Both methods overcome the kinetic barriers and require that α-LA undergoes a partially unfolded conformational change to bind to OA, in which motifs are exposed to the solvent and act as structurally stabilizing cofactors through hydrophobic interactions[27]. The less-restrained partially unfolded state from the synthesis of $AuQC_{705}$ (Fig. 2g) has rendered the formation of $AuQC_{705}$–BAMLET lipoprotein nanocomplex feasible and can be used to provide macroscopic and microscopic image guidance to track intratumoural drug distribution patterns. 8-anilinonaphthalenesulfonate (ANS) spectra of $AuQC_{705}$ with a hypsochromic shift and increased intensity interpreted a higher surface hydrophobicity compared with native α-LA, which is advantageous for OA binding (Fig. 6a). Accordingly, the intrinsic Trp fluorescence of $AuQC_{705}$ also decreased after binding to OA (Supplementary Fig. 14b). NIR fluorescence of $AuQC_{705}$ well withstands heat shock at 70 °C with a minimal decrease at physiological pH, but is appreciably quenched after interacting with OA, indicating the formation of $AuQC_{705}$–BAMLET nanocomplexes (Fig. 6a), with a ratio of OA to α-LA of 3:1 (Supplementary Fig. 37). At high pH, $AuQC_{705}$ is more vulnerable to heat shock (Supplementary Fig. 38), which intensely unfolds α-LA, exposes its hydrophobic surfaces and induces self-aggregation followed by energy-transfer quenching[45]. More significant quenching from OA binding was observed at higher pH due to intense aggregation[46]. However, physiological pH is more relevant to clinical conditions and sufficient for BAMLET conversion[45,47]. Surface hydrophobicity further increased after forming $AuQC_{705}$–BAMLET (Fig. 6a), similar to HAMLET[11].

$AuQC_{705}$–BAMLET nanocomplex against breast cancer. The in vitro anti-cancer effect of $AuQC_{705}$–BAMLET nanocomplexes was assessed in MDA-MB-231 cancer cells with approximately 95% cell death, comparable to BAMLET, whereas $AuQC_{705}$ and α-LA had insignificant effects (Fig. 6b). Positive staining for phosphatidylserine (PS)-binding annexin V and DNA-binding ethidium homodimer III (EthD-III) showed the induction of outer-membrane translocation of PS and membrane-integrity disruption by $AuQC_{705}$–BAMLET, with an increase in both early and late apoptotic/necrotic cell populations (Fig. 6c, Supplementary Fig. 39a). $AuQC_{705}$–BAMLET substantially shifted cell proportions into light scatter gates of early apoptosis and late apoptosis/necrosis, accompanied by increased fluorescence (Supplementary Fig. 39b). Through careful inspection of cell morphological progressions using time-lapse differential interference contrast (DIC) microscopy, cancer cells treated with $AuQC_{705}$–BAMLET underwent similar features of apoptosis[48], with an initial retraction of pseudopodial protrusion and cell shrinkage into a spherical shape (Fig. 6d, Supplementary Video 1). Chromatin condensation and fragmented irregular nuclei became visible at 60 min and cancer cells then proceeded to form multiple apoptotic bodies near to the cell membrane at 180 min, followed by substrate detachment and breakdown into numerous apoptotic bodies. In terms of localization, $AuQC_{705}$–BAMLET appeared to first bind to cell membranes at 120 min and then transport into the cytoplasm, with maintained membrane integrity (Fig. 6d). α-LA and $AuQC_{705}$ alone did not induce any noticeable cell death, light-scatter variations or morphological changes (Fig. 6b–c, Supplementary Fig. 39, Supplementary Videos 2–4). Most healthy control cells remained in the G0/G1 phase for preparation of DNA replication, with a negligible sub-G1 population that was representative of apoptosis and inhibition of cell cycle progression (Fig. 6e). Although both α-LA and $AuQC_{705}$ displayed a healthy pattern, $AuQC_{705}$–BAMLET induced DNA damage and dominant sub-G1 arrest in which the hypodiploid proportion increased with increasing concentrations, along with a gradually decreasing population in G0/G1. $AuQC_{705}$–BAMLET led to mitochondrial dysfunction, which is the hallmark of apoptosis, resulting in mitochondrial membrane depolarization with a significantly smaller ratio of red 5,5′,6,6′-tetrachloro-1,1′,3,3′-tetraethylbenzimidazolyl-carbocyanineiodide (JC-1) aggregates to green JC-1 monomers compared with treatment with α-LA and $AuQC_{705}$ (Fig. 6f). $AuQC_{705}$–BAMLET also severely impaired mitochondrial respiration and induced a switch to the glycolytic phenotype; cells showed an enhanced Warburg effect (Fig. 6g, Supplementary Fig. 40). The inhibition of in vivo tumour growth by $AuQC_{705}$–BAMLET was estimated by coimplanting MDA-MB-231 tumours into J:NU mice (Fig. 6h). Both $AuQC_{705}$ and $AuQC_{705}$–BAMLET were retained in the tumour area with discriminable fluorescence until the fifth day, indicating that diffusion to adjacent healthy tissues was largely prevented (Supplementary Fig. 41). Moreover, neither α-LA nor $AuQC_{705}$ was able to suppress tumour growth compared with the control, whereas no palpable tumours were present for $AuQC_{705}$–BAMLET 30 d after implantation (Supplementary Fig. 42). We next administered $AuQC_{705}$–BAMLET in situ in mice bearing dual orthotopic triple-negative MDA-MB-231/468 tumours in the mammary fat pads, as they typically lack the three most successful therapeutic receptor targets. Whole-body fluorescence imaging revealed the distribution of $AuQC_{705}$–BAMLET in tumours, and the areas of fluorescence matched the histology of successfully treated (necrotic) tumour areas, whereas the still viable, insufficiently treated areas were fluorescence negative (Fig. 6i). These results imply that the image guidance can be used to assess intratumoural distribution of drug load and advise the need for a follow-up readministration for untreated tumour regions. Healthy differentiated cells with low intrinsic Ras/MAPK activities were reported to be insensitive to HAMLET treatment[49]. To validate the anti-tumourigenic specificity, we subcutaneously injected $AuQC_{705}$–BAMLET into J:NU mice and found a predominant retention in the hypodermis layer rather than epidermis and dermis, primarily in papillae of hair follicles, blood-lymphatic vessels and subcutaneous ductal glands, such as the sweat and mammary glands (Supplementary Fig. 43). Skin histology remained similar to healthy skin without any noticeable thickening or thinning, suggesting that $AuQC_{705}$–BAMLET largely spared differentiated tissues.

Molecular mechanisms of action of $AuQC_{705}$–BAMLET. From dose–response curves of representative targets as a broad kinase inhibitor, $AuQC_{705}$–BAMLET has a lower half-maximum inhibitory concentration (IC_{50}) for activin-receptor like kinase 1 (ALK1) and B-Raf proto-oncogene serine/threonine protein kinase (BRAF) compared with epidermal growth factor receptor (Supplementary Fig. 44). To investigate the intricate underlying anti-cancer molecular mechanism of $AuQC_{705}$–BAMLET, we examined a number of key signalling pathways using large-scale radiometric functional kinome profiling against a full panel of 369 wild-type recombinant human protein kinases by quantifying [γ33P]ATP release (Fig. 7a). Similar to HAMLET[50], $AuQC_{705}$–BAMLET elicited multitargeted kinase inhibition at all branches of the kinome dendrogram, but significant variations for several individual kinases were observed (Fig. 7b,c). Its broad spectral kinase inhibition showed no correlation with any well-established kinase inhibitors (Supplementary Fig. 45e). To functionally characterize the spectrum of targeted kinome by $AuQC_{705}$–BAMLET, the most inhibited human kinases (≥95%) were selected and analysed using functional enrichment analysis. The most enriched Gene Ontology (GO) slim terms within the enrichment landscape included ‘immune system process’, ‘cellular protein modification’ and ‘signal transduction’, and ‘response to stress’ and ‘cell cycle and cell death’ (Supplementary Fig. 46a,b). This suggests that the actions of $AuQC_{705}$–BAMLET encompass perturbations in proliferative signalling pathways, inductions of cell death and stress responses, as demonstrated

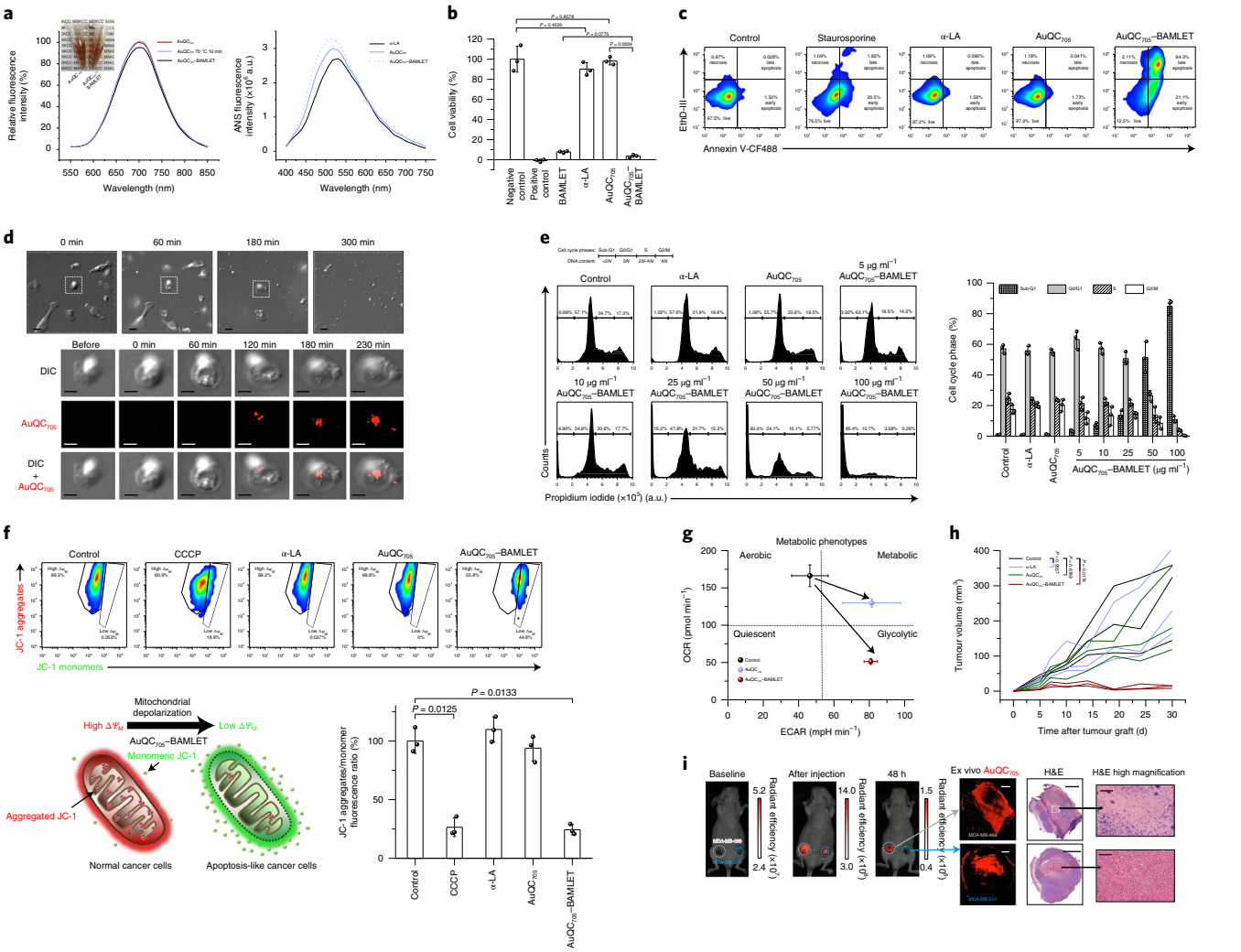

Fig. 6 | AuQC$_{705}$–BAMLET is a potent nanocomplex for inducing cancer cell death. a, Fluorescence spectra of AuQC$_{705}$, AuQC$_{705}$ after 10 min heat shock at 70 °C and AuQC$_{705}$–BAMLET at pH 7 (left). Inset: decrease in optical transparency after formation of AuQC$_{705}$–BAMLET. Right, ANS spectra of α-LA, AuQC$_{705}$ and AuQC$_{705}$–BAMLET, reflecting surface hydrophobicity. a.u., arbitrary units. **b**, The viability of MDA-MB-231 cancer cells after 3 h treatment of BAMLET (2 mg ml^{-1}), α-LA (2 mg ml^{-1}), AuQC$_{705}$ (100 μg ml^{-1}) and AuQC$_{705}$–BAMLET (100 μg ml^{-1}); $n = 3$ biologically independent samples. For the positive control, 1 mM SDS was used. **c**, Flow cytometry analysis of MDA-MB-231 cells that were stained with annexin V-CF488 (excitation, 488 nm; emission, 530/50 nm band pass (BP)) and EthD-III (excitation, 532 nm; emission, 610/20 nm BP) for early apoptosis and late apoptosis/necrosis, respectively, after 3 h treatment of α-LA, AuQC$_{705}$ and AuQC$_{705}$–BAMLET (75 μg ml^{-1}). Staurosporine (5 μM) was used as an apoptosis-inducing control. The percentage of cells in each quadrant is indicated. **d**, Time-lapse DIC microscopy of MDA-MB-231 cells treated with 250 μg ml^{-1} AuQC$_{705}$–BAMLET (top). Bottom, morphological and intracellular fluorescence analysis of a single cell. Scale bars, 20 μm (top row) and 10 μm (bottom three rows). **e**, Cell cycle analysis by quantifying DNA content using the intracellular DNA-binding dye propidium iodide (excitation, 532 nm; emission, 610/20 nm BP); $n = 3$ biologically independent samples. MDA-MB-231 cancer cells were treated with 2 mg ml^{-1} α-LA, 100 μg ml^{-1} AuQC$_{705}$ and 5–100 μg ml^{-1} AuQC$_{705}$–BAMLET for 1 h. The percentage of cells is indicated on the plot for cell cycle phases of sub-G1, G0/G1, S and G2/M corresponding to DNA content of $<2N$, $2N$, $2N$–$4N$ and $4N$, respectively (left). Right, the percentage of each cell cycle phase. **f**, Flow cytometry analysis of mitochondrial membrane potentials ($\Delta\Psi_M$) using lipophilic cationic JC-1 with 100 μM carbonyl cyanide 3-chlorophenylhydrazone (CCCP) as a positive control; $n = 3$ biologically independent samples. The top left gate represents normal mitochondria in healthy cells with high $\Delta\Psi_M$, intense in red fluorescence (excitation, 532 nm; emission, 610/20 nm BP) from JC-1 aggregates. The cell population in the bottom right gate has low $\Delta\Psi_M$ with green fluorescence (excitation, 488 nm; emission, 530/50 nm BP) from monomeric JC-1. The schematic shows the shift of red fluorescence of JC-1 aggregates into green fluorescence of JC-1 monomers by AuQC$_{705}$–BAMLET, causing mitochondrial depolarization (bottom left). The ratio of JC-1 aggregates to monomers (red/green fluorescence ratio) is a sensitive indicator of mitochondrial membrane polarization (bottom right)**. g**, Cell energy phenotype diagram showing phenotypic switching of MDA-MB-231 cells from the baseline control by AuQC$_{705}$ and AuQC$_{705}$–BAMLET; $n = 2$ biologically independent samples. OCR, oxygen consumption rate; ECAR, extracellular acidification rate. **h**, Tumour growth patterns of MDA-MB-231 human xenografts co-implanted with AuQC$_{705}$–BAMLET. AuQC$_{705}$–BAMLET showed statistically significant growth inhibition compared with the control group, whereas no significance was found for either α-LA or AuQC$_{705}$; $n = 3$ biologically independent animals. **i**, Localized anti-cancer therapy guided by NIR-fluorescence images in dual orthotopic MDA-MB-231/468 breast cancer models using AuQC$_{705}$–BAMLET. The unit of radiant efficiency is photons s^{-1} cm^{-2} sr^{-1} (μW cm^{-2})$^{-1}$. No AuQC$_{705}$-specific signals were detected at the baseline. AuQC$_{705}$–BAMLET induced potent cell death and was confined within the tumours, as visualized by fluorescence. Spatially defined drug distribution within the tumours was revealed by ex vivo microscopic imaging after identical in vivo imaging patterns were observed in both of the tumours, and was in agreement with the histopathology analysis. Newly differentiated viable cancer cells have low AuQC$_{705}$ signals, whereas strong signals from AuQC$_{705}$–BAMLET correlate well with cell death. One enlarged region of cell death is presented for each tumour. H&E, haematoxylin and eosin. Scale bars, 1,000 μm (left), 2,000 μm (middle) and 100 μm (right).

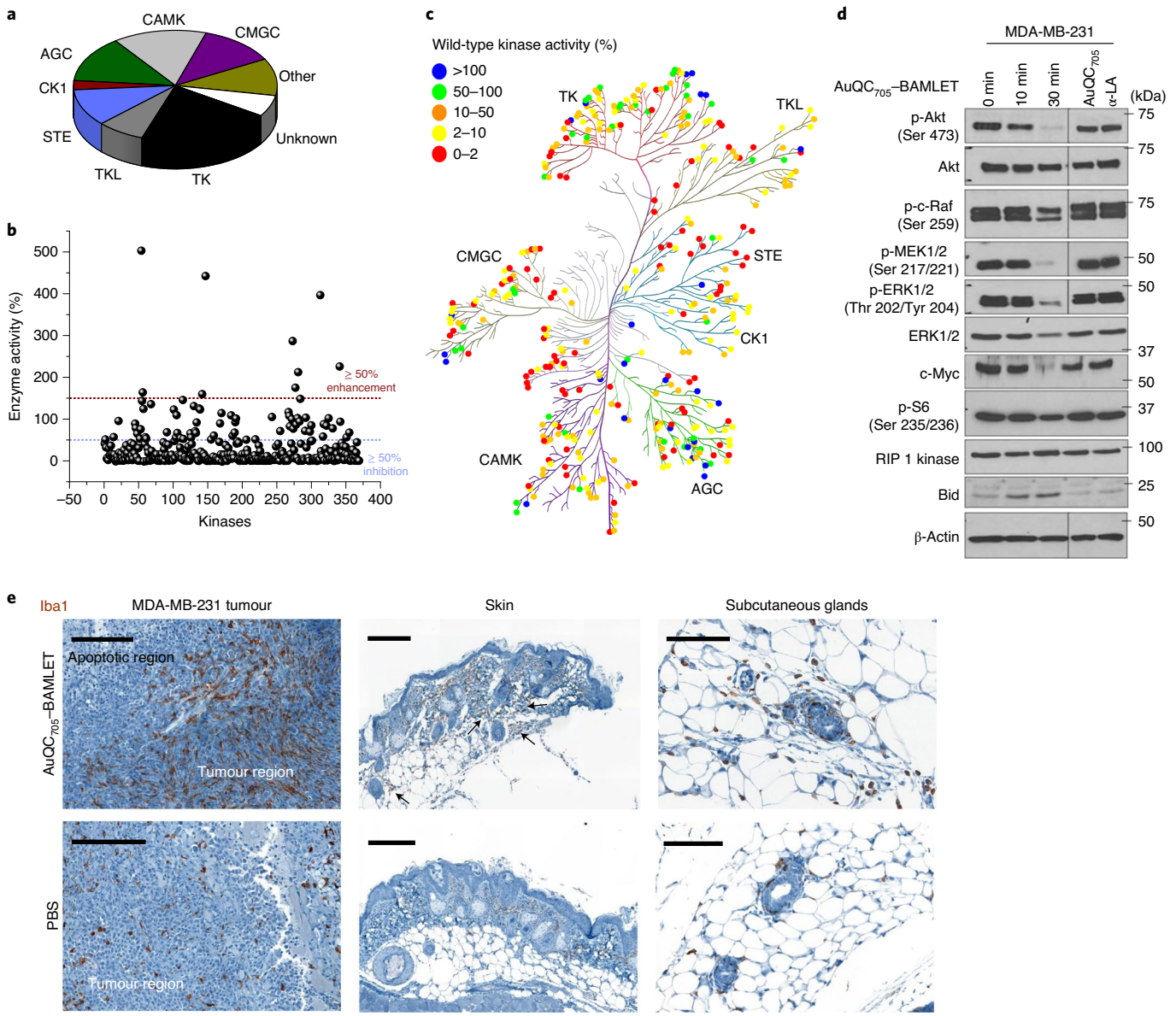

Fig. 7 | Molecular mechanisms of anti-cancer AuQC$_{705}$–BAMLET lipoprotein nanocomplex. a, The distribution of all of the wild-type human kinases in the screening panel. They are classified into nine groups as follows: protein kinases A, G and C (AGC), calmodulin/calcium-dependent kinases (CAMK), casein kinase 1 (CK1), CDK, MAPK, GSK3 and CLK (CMGC), homologues of yeast sterile 7, 11 and 20 (STE), tyrosine kinase (TK), tyrosine kinase-like (TLK), other (not belong to any of the above kinase families) and unknown (kinase-partner complexes and isoforms that could not be mapped on kinome tree). **b**, Kinase inhibition by AuQC$_{705}$-BAMLET. Wild-type human kinases can be broadly inhibited (≥ 50% inhibition). **c**, Human kinome dendrographic mapping of kinase targets of AuQC$_{705}$-BAMLET. Each dot in the dendrogram indicates an individual kinase and each branch represents a kinase group. The strongest inhibition is shown in red and enhancement is shown in blue. **d**, Western blots of molecules involved in cell-death regulatory signalling pathways. β-Actin was used as the internal loading control. Molecular mass markers are labelled on the right. p-, phosphorylated protein. **e**, IHC staining of macrophage-specific ionized calcium-binding adapter molecule 1 (Iba1) for MDA-MB-231 breast tumours, skin tissues and enlarged subcutaneous glands. Tissues were resected from J:NU xenograft mice 24 h after intratumoural or subcutaneous injection of AuQC$_{705}$-BAMLET (150 μg) or PBS. Macrophage-enriched areas of subcutaneous glands are indicated by black arrows. Scale bars, 200 μm (left and middle) and 100 μm (right).

above. To further understand how perturbed genes affect functional changes in pathways, we mapped perturbed kinases to the Kyoto Encyclopedia of Genes and Genomes (KEGG) pathway database and found that MAPK and PI3K–AKT are notably affected signalling pathways that regulate cell survival, proliferation and apoptosis (Supplementary Fig. 46c,d).

To further validate the impact of AuQC$_{705}$–BAMLET on individual protein levels and their post-translational modifications, especially phosphorylation, we performed reverse-phase protein array (RPPA) profiling of the imperative effectors that coordinate cellular signals. AuQC$_{705}$ and α-LA did not significantly alter the proteomic pattern compared with the control, whereas AuQC$_{705}$–BAMLET elicited major alterations in the cancer proteome (Supplementary Fig. 46e). A number of tumour suppressors, growth-inhibitory and proapoptotic proteins, such as Smad4, GATA3, VHL, Merlin, Smac, INPP4B and p16INK4a, were prominently upregulated[51–55]. Importantly, observed increases in claudin-7 and Notch3 indicate inhibitory effects of AuQC$_{705}$–BAMLET on epithelial to mesenchymal transition (EMT)[56,57]. Concomitantly, proteins that promote angiogenesis, exacerbate invasiveness, antagonize apoptosis, sustain cancer survival and

metabolism were downregulated, including eIF4G, PKM2, Tuberin, TRIM25, eEF-2K, YAP, FAK, JNK2, ATM, mTOR, 14-3-3ζ and DJ-1 as well as phosphorylated PKCβII, AMPKα, ACC and 4E-BP1 (refs. [58–70]). To better elucidate a suggestive mechanism of action, we combined RPPA and kinome profiling and incorporated them into a signalling map focusing on MAPK and PI3K pathways (Supplementary Fig. 46f). The level of phosphorylated and total MEK/ERK and the downstream p38 were strongly inhibited, indicating perturbation of proliferative pathways[71]. $AuQC_{705}$–BAMLET also oppositely regulates c-Jun N-terminal kinase 1 (JNK1) and JNK2 to activate JNK–c-JUN mediated apoptosis[72]. We also observed inhibition of the nuclear factor kappa B (NF-κB) pro-inflammatory cascade through canonical, noncanonical and IKK-independent atypical pathways, endowed by inhibiting activities of survival-promoting IκB kinase (IKK) complex (IKKα and IKKβ), CK2, p38-MAPK and phosphorylated NF-κB p65 subunit[73,74] (Supplementary Fig. 46g).

Next, we used biochemical approaches to verify the effect of $AuQC_{705}$–BAMLET in the proliferation- and survival-promoting MAPK and PI3K–Akt signalling pathways (Fig. 7d, Supplementary Fig. 47). We observed a significant decrease in the Akt phosphorylation at Ser 473 and ribosomal protein S6 in the PI3K–Akt signalling cascade after exposure to $AuQC_{705}$–BAMLET, with total Akt expression barely altered. Similarly, $AuQC_{705}$–BAMLET had negative impact on MAPK–ERK-mediated signal transduction, with a noticeable decrease in phosphorylation of Ras-activated MEK1/2, c-Raf and ERK1/2 as well as downstream c-Myc. Downregulation of oncogenic c-Myc was closely related to apoptosis induction[75] and Raf isoform c-Raf was reported to delay mitochondrial membrane depolarization and antagonize apoptosis[76]. The proapoptotic Bid, which in turn activates mitochondrial apoptotic regulator Bax, was upregulated, whereas the level of RIP1 kinase in the necroptosis pathway was barely affected.

Simultaneous inhibitions of major tumorigenesis pathways by a single therapeutic agent restrain the ability of cancer cells to utilize alternative signalling pathways to survive and therefore overcome the frequently occurring problem of drug resistance. As shown by GO analysis (Supplementary Fig. 46a), modulation of immune system processes by $AuQC_{705}$–BAMLET favouring tumour suppression is intriguing. Using immunohistochemistry (IHC) staining for the macrophage-specific pan marker ionized calcium-binding adapter molecule 1 (Iba-1), we found prevalent recruitment of numerous macrophages infiltrating the tumour near to the apoptotic area induced by $AuQC_{705}$–BAMLET, whereas only a few scattered macrophages were observed in the control tumour that was injected with PBS (Fig. 7e). Subcutaneous injection of $AuQC_{705}$–BAMLET also recruits more macrophages into the dermis and hypodermis layers compared with the controls and the contralateral side (Fig. 7e, Supplementary Fig. 48). These granulated macrophages tend to move towards subcutaneous glands where uptake of $AuQC_{705}$–BAMLET is high (Fig. 7e, Supplementary Fig. 43b). $AuQC_{705}$–BAMLET elicited immunogenic cancer cell death through rapid surface translocation of calreticulin (CRT; Supplementary Fig. 49), which determines anti-cancer immune responses[77]. α-LA was reported to positively regulate IL-1β secretion promoting M2 to M1 phenotype of macrophages[78], and was used for breast cancer vaccination through autoimmunity[18]. Such immune infiltration could modulate the tumour microenvironment and homeostasis, including a switched polarization against cancer[79]. However, the significance of macrophage recruitment and detailed immuno-oncological mechanisms need future investigations. Finally, the immunogenicity is significantly decreased for $AuQC_{705}$ and $AuQC_{705}$–BAMLET compared with native α-LA (Supplementary Fig. 50), owing to the partially unfolded structure during synthesis[80].

Outlook. For many cancers such as breast cancer, optimal treatment relies on visualization of the overall tumour extent in the body using whole-body imaging. After this initial staging, surgery is the mainstay of therapy in most cases. In this case, it is highly desirable to be able to visualize the true local tumour extent with an imaging modality that can be performed in the operating room or in resource-limited settings. As the next major step in patient treatment, one would ideally be able to destroy all tumour tissues by local injection of a therapeutic agent, obviating the need for systemic chemotherapy or radiation therapy, which are limited by their side effects and are still hampered by their often-limited benefit for patient survival.

Although many imaging or therapeutic agents have been reported that are able to address one or more of these goals, an integrated approach in which one agent can deliver all of the above is lacking. With this goal in mind, we designed, synthesized and validated an ultrasmall multifunctional nanoprobe that provides (1) whole-body imaging detection of breast cancer with MRI and CT, (2) local imaging of tumour extent using fluorescence and (3) potent local antitumour therapy. Furthermore, this agent is (4) ultrasmall (<6 nm hydrodynamic diameter), enabling renal clearance, and (5) consists of biocompatible components, most of which have already been validated in clinical trials. Both (4) and (5) are crucial to ultimate clinical translation. We further envision that this approach will stimulate emerging paradigms for the rational design of nanomedicines.

Methods

Reagents. Gold chloride trihydrate ($HAuCl_4 \cdot 3H_2O$, G4022), FITC–dextran (20 kDa, ~3.3 nm, FD20S), cell culture-grade dimethyl sulfoxide (DMSO, D4540) and D-glucosamine (2DG, G4875) were purchased from Sigma-Aldrich. High-purity bovine α-LA (*Bos taurus*) was provided by Agropur (Ca^{2+} < 0.055%). The purity was further verified by SDS–PAGE on a Novex NuPAGE (NP0335PK2, Invitrogen) 4–12% Bis-Tris precast protein gel using SimplyBlue SafeStain solution (LC6065, Invitrogen) for Coomassie Brilliant Blue G-250 staining. EIPA (3378) and cytochalasin D (1233) were obtained from Tocris Bioscience. NVP-BEZ235 (SYN-1018), wortmannin (AC32859) and staurosporine (ALX-380-014) were bought from AdipoGen, Acros Organics and Enzo Life Sciences, respectively. Sulfo-Cy5.5 NHS ester was purchased from Lumiprobe. Methanol-free paraformaldehyde (PFA; 16%, 0219998380) was bought from MP Biomedicals. All of the chemicals were analytical grade unless otherwise noted. Ultrapure 18.2 MΩ-cm Milli-Q water was used throughout the study. All PBS used in the study was 1× and diluted from 10× stock (BP3994, Thermo Fisher Scientific) as Ca^{2+} and Mg^{2+} free 11.9 mM pH 7.4 with 137 mM NaCl and 2.7 mM KCl, unless otherwise specified.

Synthesis of AuQCs. We established a standardized recipe with slightly different synthesis conditions in terms of pH, ratio of Au precursor to α-LA ligand and reaction time that can achieve primary tricolour fluorescence emissions at the same excitation, on the basis of a previous study with some modifications[81]. In a typical synthesis of blue light emissive $AuQC_{450}$, equal volumes of 40 mg ml^{-1} α-LA and 10 mM $HAuCl_4$ were mixed and vortexed vigorously, forming insoluble light-yellow precipitates. HCl (1 M) was added to the mixture at 30% (v/v) and vortexed until the precipitates fully dissolved. The reaction then proceeded with shaking (300 r.p.m.) at 40 °C for 2 h, sufficient to thermally unfold the native structure of α-LA[82]. Synthesis of green emissive $AuQC_{520}$ was accomplished by mixing an equal volume mixture of 10 mM $HAuCl_4$ and 10 mg ml^{-1} α-LA, followed by addition of 1 M HCl at 30% (v/v). The mixture was vortexed and kept at 300 r.p.m. at 40 °C for 252 h with precipitates removed by centrifugation after reaction. For the far-red-NIR emissive $AuQC_{705}$, 1 M NaOH was added to an equal volume mixture of 40 mg ml^{-1} α-LA and 10 mM $HAuCl_4$ at 15% (v/v) and the solution was vigorously vortexed until precipitates disappeared. The reaction was allowed for 20 h at 300 r.p.m. at 40 °C. After synthesis, potential large particles were removed by centrifugation. For injections, $AuQC_{705}$ was exchanged into 1× PBS pH 7.4 by dialysis in a Slide-A-Lyzer 10 kDa cassette (66830, Thermo Fisher Scientific) for 48 h, protected from light with fresh buffers replaced every 8 h. It was then concentrated in a 10 kDa Amicon centrifugal filter (UFC901024, Millipore). These procedures also removed a small portion of stabilizing α-LA ligands verified by bicinchoninic acid (BCA) assay kits (23225, Pierce), to reduce viscosity suitable for injections accompanied by minor hypsochromic shifts in fluorescence emission. As AuQCs are in the form of complexes, all concentrations in this study refer to Au mass weight unless otherwise noted. AuQCs were mixed at approximate fluorescence intensity ratios to achieve desired fluorescence colours.

Blocking and quantification of sulfhydryls on α-LA. α-LA (5 mg ml^{-1}) was dissolved in 50 mM HEPES pH 7.5 containing 18 mM Tris(2-carboxyethyl) phosphine hydrochloride (TCEP-HCl, 20490, Pierce). The reduction reaction was

maintained at room temperature on a rotator for 2 h and dialysed in a 3.5 kDa cassette to remove excessive TCEP. Freshly equilibrated *N*-ethylmaleimide (NEM; 30 mM; 23030, Pierce) was added to react with solvent-exposed sulfhydryls for 2 h at room temperature to form stable thioether bonds. The thiol-blocked α-LA was further dialysed at 3.5 kDa cut-off against PBS to remove excessive NEM. Solvent-exposed sulfhydryl groups in native, TCEP-reduced and NEM-blocked α-LA were quantified by Ellman's assays using 5,5′-dithio-bis-(2-nitrobenzoic acid) (DTNB, 22582, Pierce). L-cysteine hydrochloride monohydrate was used as standards from 0–1.5 mM. DTNB (50 µl of 4 mg ml^{-1}) and 250 µl samples or standards were added to 2.5 ml PBS and mixed on a rotator for 15 min at room temperature, and then absorbance was measured at 412 nm. Thiol-blocked α-LA was lyophilized and reconstituted for further use.

Synthesis of 10.6 nm and 2.5 nm AuNPs. AuNPs (10.6 nm) were synthesized by quickly adding 15 ml 1% w/w citrate to 100 ml boiling 1 mM $HAuCl_4$ with stirring at 400 r.p.m. Continuous boiling was retained for 15 min until the colour turned wine red. The solution was then cooled to room temperature with stirring and filtered through a 0.22 µm membrane. Ultrasmall 2.5 nm AuNPs were synthesized as previously reported with some modifications[83]. THPC (1.2 ml of 80%) was added to 100 ml water, 1 ml of which was then added to 45 ml water with vigorous stirring for 5 min. NaOH (2.5 ml of 0.2 M) was added, followed by quick introduction of 588 µl 0.1 M $HAuCl_4$. An immediate colour change to dark brown could be observed and the reaction was maintained in a lightproof container with stirring overnight. NPs were characterized using SeaKem GTG agarose (50070, Lonza) gel electrophoresis (0.5% in 0.5× TBE buffer) running at 60 V for 30 min.

Evaluation of individual amino acids in α-LA. To determine the potential contribution from each amino acid residue of α-LA in the fluorescence emission of AuQCs, all 20 amino acids in the primary structure including alanine, cysteine, aspartic acid, glutamic acid, phenylalanine, glycine, histidine, isoleucine, lysine, leucine, methionine, asparagine, proline, glutamine, arginine, serine, threonine, valine, tryptophan and tyrosine were studied. Cystine ($(Cys)_2$) and hydroxyproline (*trans*-4-hydroxy-L-proline) were also investigated for effects of disulfide bonds and proline hydroxylation. Amino acids with low solubility were mildly heated or sonicated until complete dissolution or homogeneous suspension was acquired. Reactions containing 20 mg ml^{-1} amino acids and 5 mM $HAuCl_4$ were performed at 40 °C for 20 h after adding HCl or NaOH as described above.

Characterization of AuQCs. Steady-state intrinsic Trp fluorescence was recorded in a quartz cuvette using SpectraMax M5 (Molecular Devices) at 295 nm excitation to minimize tyrosine fluorescence. Fluorescence of AuQCs was measured using a SpectraMax Paradigm (Molecular Devices) in an ultrathin low-background-fluorescence black 96-well plate (3720, Corning). PLE was measured in 5 nm steps. Transmission electron microscopy (TEM) images were acquired using a JEOL 1200 EX transmission electron microscope operating at 80 kV on a 300-mesh carbon-film-coated copper grid (CF300-Cu, Electron Microscopy Sciences). Hydrodynamic size from dynamic light scattering and zeta potential were determined using a Zen 3600 Zetasizer Nano System (Malvern). CD spectra were measured using a Aviv Circular Dichroism Model 62DS (Aviv Biomedical) at room temperature in PBS and secondary structure compositions were determined using the β-structure selection approach (BeStSel)[84]. AFM was performed in 20 mM pH 6.8 HEPES containing 5 mM $MgCl_2$ deposited on mica (01874, SPI) under tapping mode at room temperature on Asylum Research MFP-3D-BIO (Oxford Instruments). Olympus AC240TS-R3 AFM probe (resonance frequency, 70 kHz; spring constant, 1.7 N m^{-1}) and Nanosensors SSS-SEIHR AFM probe (resonance frequency, 135 kHz; spring constant, 21 N m^{-1}) were used to record low- and high-resolution images at 0.5–1 Hz. MALDI–TOF-MS was conducted using an Autoflex high-performance MALDI–TOF system (Bruker Daltonics). A MALDI matrix solution was prepared in a 1:3 (v/v) mixture of acetonitrile and 0.1% aqueous trifluoroacetic acid with sinapinic acid as the ionization matrix. The sample (2 µl) was added to 40 µl MALDI matrix for 1 s mild sonication and 1 µl of the mixture was spotted onto the target (Bruker MTP 384 MALDI target) using the dried-droplet method. Approximately 250 shots of 35–40% laser were used for ionization and averaged with spectra collected in positive-ion mode. The number of Au atoms embedded in the α-LA scaffold was calculated on the basis of the *m*/*z* peak shifts. Thermogravimetric analysis was performed using the TG 209 F1 Libra system (Netzsch Instruments).

Reproducibility, stability and QY. Batch-to-batch reproducibility was determined by measuring the fluorescence spectra of three individually synthesized batches. Photostability of AuQCs was determined by continuous excitation at 360 nm for 1 h. Fluorescence stabilities were tested in 50% volume mixtures of different solutions at different time points after incubation at 37 °C. Relative QYs of AuQCs were measured using quinine sulfate (AS-80040, AnaSpec) in 0.1 M H_2SO_4 (54.6%) as the fluorescence reference standard[85]. We further confirmed the relative QY of $AuQC_{705}$ using Cy5.5-NHS ester (27020, Lumiprobe) with a similar emission wavelength. Five different concentrations around or below optical density (OD) of 0.1 (approximately 0.02, 0.04, 0.06, 0.08 and 0.1) were measured to avoid reabsorption effects. Fluorescence intensity at 360 nm excitation was integrated and plotted against absorbance. QYs were derived by comparing slopes according to the following equation:

$$\Phi_{\mathrm{AuQCs}} = \Phi_{\mathrm{ref}}\left(\frac{m_{\mathrm{AuQCs}}}{m_{\mathrm{ref}}}\right)\left(\frac{n_{\mathrm{AuQCs}}}{n_{\mathrm{ref}}}\right)^2$$

where Φ denotes QY, n refers to solvent refractive index and m is the slope.

Cell lines and culture. All of the cell lines were acquired from American Type Culture Collection (ATCC) and were routinely verified for mycoplasma contamination using MycoAlert kit (LT07-318, Lonza). MDA-MB-231 (derived from human mammary gland adenocarcinoma) and BxPC-3 (derived from human pancreas adenocarcinoma) were cultured in RPMI medium with 1 mM sodium pyruvate and 1.5 g l^{-1} sodium bicarbonate. MDA-MB-468 (derived from human mammary gland adenocarcinoma) was cultured in 1:1 mixture of DMEM (high glucose) and Ham's F-12 Nutrient Mixture with non-essential amino acids. All medium were supplemented with 10% fetal bovine serum, 2 mM L-glutamine, 1% penicillin and streptomycin. Murine mammary carcinoma 4T1 cells were cultured in RPMI with 10% fetal bovine serum, 1% penicillin and streptomycin. All cells were grown at 37 °C in a humidified atmosphere of 5% CO_2 and passaged twice a week. All cell counting in this study was achieved using a Countess automated cell counter (Invitrogen) in a counting chamber slide after staining with 0.4% trypan blue. All culture media were prepared in house by the Media Preparation Core at MSKCC.

Cell viability assay. Cell proliferation and viability were estimated using the conventional colourimetric MTT (3-(4,5-dimethylthiazol-2-yl)-2,5-diphenyltetrazolium bromide) assay (10009365, Cayman Chemical). In brief, ~2.5×10^4 cells per well were seeded in 96-well plates and cultured at 37 °C in the CO_2 incubator for 24 h. After treatment under different conditions, 10 µl MTT was added to each well followed by 4 h incubation at 37 °C to enable production of crystalline formazan in live cells. SDS (100 µl of 10%) in 0.01 M HCl was then added and further incubated for 18 h at 37 °C. Absorbance was measured at 570 nm using a plate reader with 630 nm as reference. Values were normalized to untreated controls with media controls subtracted.

qPCR with reverse transcription. For quantitative PCR (qPCR) of all cellular mRNAs, total RNA was isolated with TRIzol (15596026, Invitrogen). Total RNA (1 µg) was reverse transcribed to generate cDNA using PrimeScript RT Master Mix (RR036, TaKaRa Bio) and qPCR was performed using the RealStar Green Fast Mixture (A301, GenStar) with the indicated primers for the CFX96/384 Touch real-time PCR detection system (Bio-Rad). The mRNA expression levels were calculated with the relative quantification method $2^{-\Delta\Delta C_T}$ and determined with reference to β-actin mRNA levels.

The oligonucleotide primers used here were as follows: mKras forward, 5′-TAGACACGAAACAGGCTCAGG-3′ and reverse: 5′-GCATCGTCAACACCCTGTCT-3′; hKras forward, 5′-ACTGGGGAGGGCTTTCTTTG-3′ and reverse: 5′-GCATCATCAACACCCTGTCT-3′; mActin forward, 5′-AGAGGGAAATCGTGCGTGAC-3′ and reverse: 5′-CAATAGTGATGACCTGGCCGT-3′; hActin forward, 5′-CACCATTGGCAATGAGCGGTTC-3′ and reverse: 5′-AGGTCTTTGCGGATGTCCACGT-3′.

In vitro cellular uptake. In vitro cellular uptakes were accomplished by seeding 1×10^5 cells in 6-well plates and stabilized for 24 h to reach 70–80% confluence. The growth medium was replaced with new medium containing 750 µg ml^{-1} AuQCs and incubated for 12 h at 37 °C in the CO_2 incubator. Cells were detached with 0.25% trypsin and 0.05% EDTA in PBS, washed twice with PBS and immediately analysed by flow cytometry using a BD LSR II flow cytometer (BD Biosciences) under a 355-nm-excitation laser with 450/50 nm band-pass and 670 nm long-pass filters for $AuQC_{450}$ and $AuQC_{705}$, respectively. $AuQC_{520}$ was measured using a 405 nm laser with 525/50 nm band-pass filter. All flow cytometry data were analysed using FlowJo v.10. Direct and competitive uptakes were evaluated in 24-well plates with cells starved for 2 h in serum-free medium. Media containing different concentrations of $AuQC_{705}$ (0–2,000 µg ml^{-1}) or different concentrations of α-LA competitive ligands (0–40,000 µg ml^{-1}) plus 200 µg ml^{-1} $AuQC_{705}$ were added to each well to replace starvation medium and incubated at 37 °C for 2 h. Cells were fixed with 4% PFA and scanned using an IVIS Spectrum fluorescence imaging system (PerkinElmer) at 430 nm excitation and 700 nm emission. The signals of controls without $AuQC_{705}$ were subtracted.

Cell trafficking. Pharmacological inhibitor assays were performed in 12-well plates by pretreating cells with EIPA (150 µM), wortmannin (100 ng ml^{-1}), NVP-BEZ235 (4 µM) and cytochalasin D (20 µg ml^{-1}) for 1 h. $AuQC_{705}$ was added to a final concentration of 750 µg ml^{-1} and further incubated for 12 h. Cells treated with an equal amount of cell culture grade DMSO were included as a control. FITC–dextran (Sigma-Aldrich) with a molecular mass of approximately 20 kDa and a hydrodynamic size of 3.3 nm, both of which are similar to $AuQC_{705}$, was used as the

macropinocytosis marker. Cells were seeded and stabilized in four-well Lab-Tek II chambered coverglass (155382, Thermo Fisher Scientific), incubated with 500 μg ml^{-1} FITC–dextran and 375 μg ml^{-1} AuQC$_{705}$ for 0–120 min and fixed with 4% PFA before imaging. Fluorescence images were taken using a Leica TCS SP8 point-scanning inverted confocal microscope (Leica Microsystems) equipped with a tunable white-light laser source, an avalanche photodiode detector for NIR-fluorescence detection and a cell incubation chamber. 2D and 3D confocal images were analysed using Imaris image analysis software (Bitplane). For ultrastructure examination, cells were washed twice with PBS and fixed in a modified Karmovsky's fixative of 2.5% glutaraldehyde, 4% PFA and 0.02% picric acid in 0.1 M pH 7.2 sodium caocdylate buffer. After a secondary fixation in 1% osmium tetroxide and 1.5% potassium ferricyanide, samples were dehydrated through a graded ethanol series and embedded in EPON analogue resin. Ultrathin sections were cut with a diamond knife (Diatome) on RMC MT7000 Ultramicrotome (RMC). Sections were contrasted with lead citrate and imaged on copper grids with TEM.

Characterization of serum interaction. Binding profiles between AuQC$_{705}$ and serum were studied using surface plasmon resonance of a ProteOn XPR36 protein interaction array system (Bio-Rad) on a ProteOn GLC sensor chip (1765011, Bio-Rad) with an alginate-polymer-modified gold surface. Degassed PBS pH 7.4 was used as the running buffer at a flow rate of 100 μl min^{-1} in all of the surface plasmon resonance experiments. GLC sensor chips were consecutively conditioned with 100 mM HCl, 50 mM NaOH and 0.5% SDS. Surface carboxyl groups were activated with freshly prepared 40 mM 1-ethyl-3-(3-dimethylaminopropyl)carbodiimide hydrochloride (03449, Sigma-Aldrich) and 10 mM *N*-hydroxysulfosuccinimide (56485, Sigma-Aldrich). AuQC$_{705}$ (10 μg ml^{-1}) in 10 mM sodium acetate pH 4.0 was used for immobilization to form a monolayer through primary amines. The surface was deactivated with 1 M ethanolamine HCl (ETA) pH 8.5 for 10 min to quench the remaining unreacted NHS groups, followed by stabilization with running buffer to remove any non-covalently-attached AuQC$_{705}$. An alginate gold surface applied with identical surface chemistry but without AuQC$_{705}$ was included and interlane spots were used as reference. Interactions of AuQC$_{705}$ with bovine serum albumin (BSA) and mouse serum were analysed after removing non-specifically captured molecules and capture stabilization. Serial dilutions of the goat anti-bovine-α-LA antibodies (A10-128, Bethyl) were used as the positive control and 1 M NaCl buffer was used for regeneration. All presented data are double referenced to a PBS blank.

Animal models. Human xenograft and wild-type animal models were performed under the protocol 06-07-011 approved by the Institutional Animal Care and Use Committees (IACUC) at Memorial Sloan Kettering Cancer Center following NIH guidelines. All of the mice were purchased from Jackson Laboratory. Outbred homozygous (*Foxn1^{nu}*/*Foxn1^{nu}*) mutant female J:NU mice of 4–6 weeks were used for tumour inoculation. Typically, 3–5 × 10^6 breast cancer cells depending on cell lines in 80 μl 1:1 (v/v) media:Matrigel mixture were injected subcutaneously through the thoracic mammary ducts into the upper-flank region. The dual orthotopic human breast cancer model was established by injecting MDA-MB-231/468 cells through ducts into the forth abdominal mammary fat pads under anaesthesia. Inbred adult BALB/cJ wild-type female mice of 12–16 weeks were used in pharmacokinetics, clearance, pathological and toxicity studies. Isoflurane inhalation (2%; Forane, 1001936060, Baxter) anaesthesia in oxygen flow were applied in all of the non-terminal animal procedures.

Synthesis of sulfo-Cy5.5-2DG and sulfo-Cy5.5/α-LA. The small-molecular NIR imaging probe sulfo-Cy5.5-2DG was synthesized by mixing a solution comprising freshly dissolved 2.3 mM sulfo-Cy5.5-NHS (23320, Lumiprobe) in DMSO and 23 mM 2DG in PBS pH 8. The reaction proceeded at room temperature for 3 h, protected from light with rotating. Preparative-scale purification was performed by injecting the reaction mixture into a Waters 2545 high-performance liquid chromatography (HPLC) system with XBridge Prep C18 reverse phase OBD column (pore size, 135 Å; length, 250 mm; particle size, 5 μm) and 2996 photodiode array detector (Waters) at a flow rate of 10 ml min^{-1}. Ultraviolet detection was set at 254 nm and a mobile phase gradient of 5–35% CH_3CN in 0.1% aqueous trifluoroacetic acid was applied. Fractions containing sulfo-Cy5.5-2DG with a retention time of 12.7 min were collected, lyophilized and redissolved in PBS. Chemical purity was examined by analytical LC–MS with electrospray ionization using an ACQUITY UPLC system (Waters) and molecules were confirmed by high-resolution electrospray ionization TOF mass spectrometry using a Micromass LCT Premier XE mass spectrometer (Waters). HRMS (ES$^-$) *m*/*z*: calculated for $C_{47}H_{52}N_3O_{18}Na_2S_4^-$ ([M + 2Na-3H]$^-$) 1120.1901, found 1120.1924. Sulfo-Cy5.5/α-LA probe was conjugated by mixing 500 μM equimolar α-LA and sulfo-Cy5.5-NHS (final DMSO, <10% (v/v) in PBS pH 8). The product was washed five times with pH 7.4 PBS in a 3.5 kDa cut-off filter, lyophilized and reconstituted. The labelling efficiency was close to 100% as evidenced by the almost colourless filtrates. The dye labelling ratio was calculated to be 1.09 per α-LA using extinction coefficients of 28,540 at 280 nm and 209,000 at 675 nm for α-LA and Cy5.5, respectively, along with an experimentally determined correction factor of 0.07; 10 nmol dye equivalence in PBS pH 7.4 was injected through the tail vein and in vivo imaging was conducted in default multispectral Cy5.5 channels.

In vivo fluorescence imaging. J:NU mice grafted with human breast tumours were intravenously (i.v.) injected with AuQC$_{705}$ (187.5 mg kg^{-1}), anaesthetized at a vaporizer and imaged using the IVIS system at 500 nm excitation and 680–800 nm emissions with 20 nm steps. For multiplexed imaging, AuQCs (7.5 mg kg^{-1} AuQC$_{520/705}$ and 15 mg kg^{-1} AuQC$_{450}$) were injected subcutaneously. The region of interest tumour area, in pixels, was determined in a free-drawn manner guided by bright-field imaging. Normal contralateral region was calculated from the mean of three selected areas with equal pixels as tumour area. Average radiant efficiency (photons s^{-1} cm^{-2} sr^{-1} (μW cm^{-2})$^{-1}$) was calculated, defined as the quantity of photons radiated per second per area of biological tissues per steradian in response to unit power density. The results were readily normalized for integration times, binning, F/stop, field of view, illumination density and pixel numbers. Autofluorescence was subtracted from these calculated values. Multispectral unmixing was performed manually in Living Image v.4.7.2 (PerkinElmer) using in vivo spectra of AuQC$_{705}$ with autofluorescence coded green. All of the fluorescence images were adjusted to optimal threshold for displaying tumours. The lines were not flushed for all injections in the study.

X-ray CT and MRI imaging. Contrast-enhanced CT imaging using AuQC$_{705}$ was performed using a NanoSPECT/CT device (Mediso Medical Imaging) operating at 65 kVp and with an exposure time of 1,500 ms at medium in-plane voxel size. AuQC$_{705}$ (1.28 g kg^{-1}) was i.v. infused with a custom-made manual catheter and imaging was performed at baseline and 1 h after injection. CT slices were reconstructed using InVivoScope; edge and bed signals were excluded. MRI scans were performed using a 7 T small animal MRI scanner (Bruker Biospin) equipped with a 12-cm inner diameter gradient coil (Resonance Research) at 640 mT m^{-1} maximum gradient amplitude and 4,600 T m^{-1} s^{-1} maximum slew rate. A custom-built 32-mm quadrature radiofrequency body coil (Starks Contrast MRI Coils Research) was used for radiofrequency excitation and detection using a Bruker Avance electronics system. For in vivo studies, 1.5 mg AuQC$_{705}$ was intratumourally injected and animal respiration during MRI was monitored by a physiological monitoring system (SA Instruments). A 3D RARE fast spin-echo-based variable TR sequence was used for T_1 mapping, with TE = 29 ms and a 128 × 64 × 16 matrix. A MSME sequence with multiple spin echo times was applied with TR = 2 s and a matrix of 128 × 96 in 1 mm slice thickness for T_2 mapping. T_1 and T_2 mapping of phantoms were acquired with TE = 19 ms and TR = 2 s, respectively. Maps were computed using the Levenberg–Marquardt fitting algorithm in ParaVision v.5.1 (Bruker Biospin) and visualized using ImageJ (National Institutes of Health).

Intraoperative imaging using a smartphone imaging prototype. Portable tumour imaging was based on the iPhone 7 Plus. A 700 ± 40 nm bandpass filter (FB700-40, Thorlabs) was used to reduce interfering light for specific detection of AuQC$_{705}$ NIR emission. A size-matching plastic restraining ring (SM1RR, Thorlabs) and a lens tube (SM1L03, Thorlabs) were assembled into an optical filter adapter customized by 3D printing (Shapeways) with black natural plastic to anchor the filter and set it onto the camera using tape. A short-wavelength 395 nm LED panel (395–400 nm) was used as a standalone component for excitation. Intraoperative surgical imaging was performed under a surgical scenario with skin removed 24 h after injection.

Pharmacokinetics, renal clearance kinetics and toxicity. For pharmacokinetic studies, BALB/cJ wild-type mice were i.v. injected with AuQC$_{705}$ (187.5 mg kg^{-1}). Whole-blood samples were collected in 20 μl K_2EDTA capillaries (19.447, Sarstedt) from the retro-orbital sinus after injection under anaesthesia. Capillaries were immediately imaged using the IVIS system; mean intensities were quantified with reference to the injection solution. Blood collected from mice injected with PBS was used as controls. For clearance studies, BALB/cJ mice were kept in individual metabolic cages after injection. Urine and faeces were separated into two 50 ml Falcon tubes. Urine from all of the cages was collected after injection and measured for volumes and mean fluorescence intensities using the IVIS system with an injection solution as reference. For the toxicity study, randomized BALB/cJ mice received PBS, α-LA or different doses of AuQC$_{705}$ (93.8 mg kg^{-1} or 187.5 mg kg^{-1}) on study day 1. Mice were then observed daily for signs of morbidity/mortality for a month and euthanized at the time points with blood collected for haematology and clinical chemistry analyses.

Long-term degradation. Tissue samples were dissected, weighed and digested in freshly prepared aqua regia (molar ratio of HNO_3:HCl of 1:3) overnight at 60 °C until complete dissolution. After evaporating excessive aqua regia, residues were redissolved and diluted in 0.1 M HCl for elemental measurements using a PerkinElmer Elan DRC-e ICP-MS system at Brooklyn College Environmental Sciences Analytical Center. Data were referenced to $HAuCl_4$ standards and normalized to the injection solution. Bismuth was used as an internal control. In vitro degradability was evaluated in artificial lysosomal fluid with an established recipe[86], composed of $MgCl_2$, NaCl, Na_2HPO_4, Na_2SO_4, $CaCl_2$, sodium citrate, NaOH, citric acid, glycine, sodium tartrate, sodium lactate and sodium pyruvate, with pH adjusted to 3 to avoid precipitation.

Histology. Animals were euthanized by CO_2 asphyxiation. Freshly excised tissues were collected and fixed in 4% PFA at 4 °C overnight, washed with PBS

for 15 min and kept in 70% ethanol at 4 °C. Paraffin embedding was performed using ASP6025 automatic tissue processor (Leica Biosystems) and sectioned at a thickness of 5 µm using a Leica RM2265 automated paraffin microtome (Leica Biosystems). Sections were stained with haematoxylin and eosin for histopathological analysis and scanned with Mirax digital slide scanner (Zeiss). Images were analysed with Pannoramic Viewer software (3DHistech). Silver staining was performed using Light Insensitive Silver Enhancer Kit (ab170733, Abcam) for visualizing $AuQC_{705}$; haematoxylin and eosin were used as the tissue contrast agents. For ex vivo microscopic fluorescence imaging, unstained mounted tissue sections from fresh frozen embedding were scanned using a ZEN widefield imaging system (Zeiss) in a serial view-by-view manner.

Immunofluorescence and immunohistochemical staining. Immunofluorescence (IF) and IHC staining was performed using a Discovery XT processor (Ventana Medical Systems). For IF, tissues were embedded by fresh-frozen preparation using Tissue-Tek O.C.T. compounds (4583, VWR) in cryomolds under a 2-methylbutane bath on dry ice. Sections (thickness, 5 µm) were generated at −20 °C using a Leica CM1950 Clinical Cryostat (Leica Biosystems). Antigens were retrieved from frozen tissue sections with CC1 buffer (950-124, Ventana Medical Systems) and the sections were blocked for 30 min with Background Buster solution (NB306, Innovex), followed by avidin-biotin blocking (760-050, Ventana Medical Systems) for 8 min. Slides were incubated with rabbit polyclonal anti-EEA1 antibodies (ab2900, Abcam, 0.8 µg ml^{-1}) or rat monoclonal anti-LAMP1 antibodies (1D4B, DSHB, 0.5 µg ml^{-1}) for 5 h, followed by 60 min incubation with biotinylated goat anti-rabbit or goat anti-rat IgG (BP-9100 or BP-9400, Vector Labs) at a dilution of 1:200. Detection was achieved using streptavidin–HRP D (DAB Map Kit, 760-124, Ventana Medical Systems) followed by incubation with Tyramide Alexa Fluor 488 (B40953, Invitrogen) according to the manufacturer's instructions with predetermined dilutions. Stained slides were counterstained with 5 µg ml^{-1} 4′,6-diamidino-2-phenylindole (DAPI) for 10 min and coverslips were applied with Mowiol mounting medium for imaging. For IHC, paraffin-embedded tissue sections were deparaffinized using EZPrep buffer (950-102, Ventana Medical Systems) followed by identical procedures as described above for IF. The staining was applied with rabbit anti-Iba1 antibodies (019-19741, Wako, 0.5 µg ml^{-1}), counterstained with haematoxylin and mounted with Permount (SP15, Thermo Fisher Scientific) for scanning using a Mirax digital scanner (Zeiss). All IF and IHC stainings were also validated by IgG isotype controls.

Generation of breast cancer PDX orthotopic models. PDX models of human breast cancer were generated by surgically transplanting freshly excised human tumour specimens as passage 0 into the third thoracic mammary fat pad of NSG mice (NOD.Cg-*Prkdc*^{scid} *Il2rg*^{tm1Wjl}/SzJ, Jackson Laboratory). Two independent PDXs of hormonal-therapy resistant and oestrogen-receptor positive breast cancer were successfully established out of five different stage IV bone-metastasized breast cancer samples from patients. Another PDX of triple-negative breast tumour was established out of two different triple-negative breast cancer bone metastasis specimens. Freshly resected tumour tissues were quickly rinsed with sterile PBS to clear off any potential bone pieces carried over from surgical resections and then immediately transplanted. Simultaneously, part of the surgical tumour specimens were also minced into 1–2 mm pieces in 10 cm sterile culture dishes in serum-free MEM medium supplemented with non-essential amino acids and antibiotics, transferred to 1–2 wells of a 24-well plate and transduced with infected cell supernatants of lentiviral vectors expressing GFP-luciferase (for triple negative) or pUltra-Chili-Luc plasmids (Addgene plasmid, 48688; for hormonal-therapy resistant and oestrogen-receptor positive) by spinoculation at 1,500 r.p.m. for 90 min at room temperature. Samples with reporter genes were incubated at 37 °C for an additional 90 min in the cell culture incubator, after which the tumour pieces were rinsed in PBS and quickly transplanted back into the same mouse to follow as PDXs. Typically, tumour growth of passage 1 PDX became evident within 1–3 weeks after grafting and continued to grow for another 4–8 weeks before tumour necrosis and metastasis occurred, depending on specific tumours and development stages at the time of surgical resection from patients. Tumour growth patterns were periodically monitored by bioluminescence signals using the IVIS system by retro-orbitally injecting 100 mg kg^{-1} D-luciferin (14681, Cayman Chemical). Tumours were collected and retransplanted into new mice following the same procedures to derive passage two PDXs. In vivo PDX passages were limited to 2–3 to best conserve original human tumour characteristics such as heterogeneity, clinical signature, malignancy, tumour architecture and vasculature. PDXs were banked as paraffin and fresh-frozen blocks as well as cryopreservation in serum with 10% DMSO. The last passage was transplanted into J:NU mice for imaging.

Preparation of $AuQC_{705}$–BAMLET. Preconditioned column chromatography and hydrothermal approaches were previously demonstrated for synthesizing cytotoxic α-LA–OA complexes[11,44,45]. Even denaturation and the holo form of α-LA were shown to form biologically active BAMLET complex[87]. We adopted the hydrothermal approach owing to its scale-up potentials. $AuQC_{705}$ (750 µg ml^{-1}) with pH adjusted to 7 was heated, mixed with 20% (v/v) OA (A195, Thermo Fisher Scientific) and incubated at 70 °C for 10 min under vigorous mixing to facilitate unfolding and binding. After being cooled to room temperature, excessive unbound OA was removed by centrifugation through its non-polar long hydrocarbon chain. Relative surface hydrophobicity was determined using 8-anilinonaphthalene-1-sulfonic acid (ANS, 401210050, Acros Organics). A solution containing 50 µg ml^{-1} ANS and 50 µg ml^{-1} α-LA in PBS was incubated for 1 h at room temperature with ANS fluorescence measured at 350 nm excitation.

Determination of OA. The concentration of unsaturated fatty acid OA in $AuQC_{705}$–BAMLET was estimated using a copper-based assay with some modifications[88]. Copper reagent containing 0.45 M aqueous triethanolamine, 50 mM acetic acid and 137.5 mM $Cu(NO_3)_2$ was added to equal volumes of $AuQC_{705}$–BAMLET or OA standards in 100 mM Tris-HCl pH 8.0. After adding 62.5% (v/v) chloroform, solutions were vortexed and centrifuged for phase separation. The organic phase was carefully collected, with 10% (v/v) of 1% (w/v) sodium diethyldithiocarbamate in 1-butanol added. Absorbance was measured at 440 nm. OA standards were prepared by dissolving in ethanol and then diluted in 100 mM Tris-HCl pH 8.0.

Apoptosis and necrosis staining. Apoptosis and necrosis were estimated using the Apoptosis and Necrosis Quantification Kit plus (30065, Biotium) according to the manufacturer's instructions. In brief, trypsinized MDA-MB-231 cells after treatment were resuspended in binding buffer at 3×10^6 cells per ml. CF488A–Annexin V and EthD-III were added to stain surface phosphatidylserine and nuclear DNA in early apoptotic and late apoptotic/necrotic cells, respectively, followed by incubation at room temperature for 15 min without light on a rotator and analysed using flow cytometry. Unstained and single-stained controls were used for compensation. Similar procedures were applied for adherent cells in four-well chambered coverglass, which were analysed using confocal microscopy after washing with binding buffers.

Cell cycle analysis. Cell cycle phases were analysed using propidium iodide staining. MDA-MB-231 cells seeded in 12-well culture plates were treated with $AuQC_{705}$–BAMLET from 5–100 µg ml^{-1} for 1 h in medium under normal cell culture conditions with 100 µg ml^{-1} $AuQC_{705}$ and 2 mg ml^{-1} α-LA for comparison. After being collected and washed with PBS, cells were fixed in drop-wise-added ice-old 70% ethanol for 4 h at 4 °C. After further washes with PBS, cells were stained with propidium iodide/RNase staining buffer (550825, BD Pharmingen) at room temperature for 30 min and immediately analysed using flow cytometry.

Evaluation of mitochondrial functions. MDA-MB-231 cells were cultured at a density of 2×10^5 per well for 24 h and treated with 50 µg ml^{-1} $AuQC_{705}$–BAMLET for 1 h at 37 °C. $AuQC_{705}$ (100 µg ml^{-1}), α-LA (2 mg ml^{-1}) and CCCP (100 µM; C2759, Sigma-Aldrich) were included as controls. After treatment, cells were washed with PBS and replaced with fresh medium. Mitochondrial membrane potential ($\Delta\Psi_M$) as an indicator of mitochondrial function was monitored using the cationic $\Delta\Psi_M$ sensor JC-1 (5,5′,6,6′-tetrachloro-1,1′,3,3′-tetraethylbenzimidazoly l-carbocyanineiodide, 10009172, Cayman Chemical). JC-1 was freshly prepared by diluting 1:10 (v/v) in 37 °C culture medium, added to each well at a volumetric ratio of 1:10 to medium and incubated at 37 °C for 30 min. Cells were collected, washed twice with PBS and resuspended in JC-1 assay buffer for flow cytometry analysis. Mitochondrial depolarization was quantified by the ratio of aggregates to monomers. Metabolic profiles were assessed by measuring mitochondrial respiration and glycolytic function using a Seahorse XFp Extracellular Flux Analyzer (Seahorse Bioscience). The Cell Mito Stress assay was performed by seeding 3×10^4 cells per well in an XFp miniplate overnight under regular culture conditions. Cells were then treated with 10 µg ml^{-1} $AuQC_{705}$–BAMLET for 1 h with pairwise comparisons to control for cells and $AuQC_{705}$. Cells were next transferred into assay medium for incubation for 1 h at 37 °C without CO_2 for pre-equilibration, followed by subsequent injection of oligomycin, carbonyl cyanide *p*-trifluoromethoxy phenylhydrazone (FCCP) and rotenone/antimycin A, with real-time simultaneous measurements of oxygen-consumption rate and extracellular acidification rate. All data were normalized to the number of cells from DAPI staining.

Immunogenicity. For immunogenicity testing, BALB/cJ mice of 6–8 weeks were subcutaneously injected over the back of neck with 150 µg $AuQC_{705}$–BAMLET. Equivalent α-LA (3 mg) and $AuQC_{705}$ were included for comparison. Two weeks after injection, sera were separated by centrifugation from retro-orbital blood, which was collected and incubated on ice for 2 h. The presence of specific antibodies in the serum was determined using an enzyme-linked immunosorbent assay (88-50400-22, Invitrogen). In brief, Corning 9018 High Bind 96-well plates were coated with 10 mg ml^{-1} α-LA in PBS at 4 °C overnight through hydrophobic interactions between polystyrene and non-polar residues of α-LA. The plate was then blocked with 10 mg ml^{-1} BSA and 0.05% Tween-20 in PBS for 3 h at room temperature on an orbital shaker. Serum diluted to 1:50 in assay buffer (PBS with 0.5% BSA and 0.05% Tween-20) was added and incubated for 1 h under shaking at room temperature. After three washes with PBS, 1× pretitrated HRP-conjugated anti-mouse IgG detection antibodies (from 250× concentrate) in assay buffer were added for an incubation of 2 h at room temperature. After washes, 3,3′,5,5′-tetramethylbenzidine substrate solution was added and the

sample was incubated for 30 min. The reaction was stopped using 1 M H_2SO_4, and optical density was measured at 450 nm. Antibody titres were performed on the equal-volume serum mixture from all of the mice injected with α-LA. Mouse IgG isotype standard at different concentrations in assay buffer was included as a control. To determine whether the cell death is immunogenic, MDA-MB-231 cells in 12-well plates were treated with different concentrations of $AuQC_{705}$–BAMLET and stained with 10 μg ml^{-1} FITC-conjugated mouse anti-human CRT antibodies 1G6A7 (NBP1-47518, Novus Biologicals) in 3% BSA-PBS for 30 min on ice and in dark conditions with intermittent mixing. Cell-surface CRT was then detected using flow cytometry after washing. For confocal microscopy, live or fixed cells were stained with 50 μg ml^{-1} anti-FITC antibodies identically as described above and then counterstained with 10 μM Hoechst 33342.

Western blot analyses. Cells were lysed in radioimmunoprecipitation buffer (50 mM Tris-HCl pH 7.5, 150 mM NaCl, 1% NP-40, 0.5% sodium deoxycholate and 0.1% SDS) supplemented with protease inhibitor mixture (4693124001, Roche Applied Science), 2 mM Na_3VO_4, 10 mM NaF and 1 mM phenylmethanesulfonyl fluoride on ice. Cell lysates were cleared by centrifugation at maximum speed and loading was normalized according to BCA relative protein quantification. Proteins were separated using 10% SDS–PAGE under reducing conditions and blotted onto nitrocellulose membranes (10600006, GE Healthcare). After electrophoresis, the membranes were blocked with 5% non-fat dry milk in PBS for 1 h and incubated overnight with the following primary antibodies at 4 °C: 1:5,000 anti-β-actin A1978 (Sigma-Aldrich); 1:1,000 anti-p-Akt (Ser 473) 9271 (Cell Signaling); 1:500 anti-Akt 9272 (Cell Signaling); 1:1,000 anti-p-c-raf (Ser 259) 9421 (Cell Signaling); 1:500 anti-p-MEK1/2 (Ser 217/221) 9154 (Cell Signaling); 1:1,000 anti-p-ERK1/2(Thr 202/Tyr 204) 4370 (Cell Signaling); 1:1,000 anti-ERK1/2 9102 (Cell Signaling); 1:500 anti-c-myc SC-764 (Santa Cruz Biotechnologies); 1:2,000 anti-p-S6 (Ser 235/236) 4858 (Cell Signaling); 1:1,000 anti-RIP1 Kinase 4926 (Cell Signaling); 1:1,000 anti-Bid 8762 (Cell Signaling). Blots were then washed on an orbital shaker and probed with respective HRP-conjugated secondary antibodies (anti-mouse secondary, NXA931, GE Healthcare; anti-rabbit secondary, 4030-05, Southern Biotech). Bands were visualized using chemiluminescence (32209, Pierce).

In vivo treatment of breast cancer using $AuQC_{705}$–BAMLET. MDA-MB-231 human breast cancer cells (5×10^6) were coimplanted subcutaneously with 3.3 μg $AuQC_{705}$–BAMLET through the mammary ducts. No randomization or blinding was performed among mice. Fluorescence imaging was used to localize $AuQC_{705}$–BAMLET after tumour graft. Tumour volumes were measured using callipers according to the ellipsoid equation, where L, W and H are the length, width and height of the tumour, respectively:

$$V = \frac{\pi}{6} L \times W \times H$$

For image-guided therapy, a single dose of 150 μg $AuQC_{705}$–BAMLET was injected into dual orthotopic MDA-MB-231/468 tumours, after tumours grew palpable around 50–75 mm^3, to visualize macroscopic and microscopic drug distribution in vivo and ex vivo.

Human kinome profiling. In vitro kinase activity profiling of a 369 wild-type kinase panel was mapped using the HotSpot radiometric assay (Reaction Biology). Specific kinase–substrate pairs with appropriate cofactors for each kinase reaction were freshly prepared in reaction buffer (20 mM HEPES pH 7.5, 10 mM $MgCl_2$, 1 mM EGTA, 0.02% Brij 35, 0.02 mg ml^{-1} BSA, 0.1 mM Na_3VO_4, 2 mM dithiothreitol and 1% DMSO) and mixed with a final concentration of 7 μg ml^{-1} $AuQC_{705}$–BAMLET using a Echo550 Acoustic Liquid Handler (Labcyte), followed by 20 min incubation at room temperature. A mixture of ATP (Sigma-Aldrich) and [γ^{33}P]ATP (PerkinElmer) with specific activity of 10 μCi μl^{-1} at a final concentration of 10 μM were added and incubated at room temperature for another 2 h before being spotted onto P81 ion exchange filter paper (Whatman). After extensively washing with 0.75% phosphoric acid, retained radioactivity was detected as kinase activity with background controls of inactive enzymes subtracted. Serial dilutions of corresponding inhibitors for each individual kinase were performed to evaluate IC_{50} as positive controls. Assays were run in duplicates for statistical analysis and referenced to vehicle controls. Raw data were acquired as the percentage of kinase activity for each individual kinase and all of the negative values were forced to zero. Individual replicates presented a high degree of reproducibility (Supplementary Fig. 45a). The absolute difference and distribution of the coefficient of variation for the kinase-$AuQC_{705}$–BAMLET pairs followed Weibull and log-normal distributions on quantile–quantile plots (Supplementary Fig. 45b,c). No outliers were detected beyond thresholds, suggesting robustness (Supplementary Fig. 45d). A control interference assay was also performed by adding $AuQC_{705}$–BAMLET after kinase reactions to rule out substrate interference from $AuQC_{705}$–BAMLET.

Functional proteomic mapping by RPPA. Treated MDA-MB-231 cells were collected by trypsinization, washed twice with PBS and lysed on ice for 20 min in lysis buffer (1% Triton X-100, 50 mM HEPES pH 7.4, 150 mM NaCl, 1.5 mM $MgCl_2$, 1 mM EGTA, 100 mM NaF, 10 mM sodium pyrophosphate, 1 mM Na_3VO_4, 10% glycerol and freshly prepared protease and phosphatase inhibitors (4906837001, Roche Applied Science)). Lysates were centrifuged at 14,000 r.p.m. for 10 min at 4 °C, and the supernatant was collected and diluted to 1.5 μg μl^{-1} based on BCA tests. Sample buffer (40% glycerol, 8% SDS, 0.25 M Tris-HCl pH 6.8, 10% (v/v) freshly added beta-mercaptoethanol) was mixed with the above lysates at a ratio of 3:1 (v/v) and boiled for 5 min and stored at −80 °C until printing. Lysates were twofold serially diluted into five concentrations, printed onto nitrocellulose-coated slides and probed with specific antibodies using tyramide-based signal amplification and DAB colourimetric visualization. Slides were scanned on a flatbed scanner, and spots were quantified using the Array-Pro Analyzer software (Meyer Instruments) from the interpolation of the standard curve of dilutions. All data were normalized to protein loading in and among samples. Each antibody staining was also verified by a quality control test.

GO enrichment analyses. False-discovery rate and enrichment ratios (odds ratios) were calculated using Fisher's exact test comparing each GO term (biological processes) of kinases (with enzyme activity reduced to <5% after drug treatment) from the kinome screen versus that of the total 20,203 documented human proteins (reviewed) from the UniProt database[89,90]. Treemap was generated in R using the package treemap[91]. The R package GSEAbase was used to query GO slim terms[92,93]. The full treemap retained GO terms that passed the following cut-offs: FDR < 0.1 and odds ratio ≥ 1.5.

Statistical analysis. Statistical analysis was performed using Microsoft Excel and OriginPro. All data are presented as mean ± s.d. unless specified otherwise. Two-tailed unpaired Student's t-tests were used to evaluate different levels of statistical significance.

Reporting summary. Further information on research design is available in the Nature Research Reporting Summary linked to this article.

Data availability

The main data supporting the results in this study are available within the paper and its Supplementary Information. The raw and analysed datasets generated during the study are too large to be publicly shared, but they are available for research purposes from the corresponding author on reasonable request.

Code availability

The custom R code for the bioinformatics is available at https://github.com/wangtaifr/Kircher2020.

Received: 9 April 2018; Accepted: 11 June 2020;
Published online: 13 July 2020

References

1. Tang, S. S. K. et al. Current margin practice and effect on re-excision rates following the publication of the SSO-ASTRO consensus and ABS consensus guidelines: a national prospective study of 2858 women undergoing breast-conserving therapy in the UK and Ireland. *Eur. J. Cancer* **84**, 315–324 (2017).
2. Kircher, M. F. et al. A brain tumour molecular imaging strategy using a new triple-modality MRI-photoacoustic-Raman nanoparticle. *Nat. Med.* **18**, 829–834 (2012).
3. Dawidczyk, C. M. et al. State-of-the-art in design rules for drug delivery platforms: lessons learned from FDA-approved nanomedicines. *J. Control. Release* **187**, 133–144 (2014).
4. Zhang, X. D. et al. Ultrasmall $Au_{10-12}(SG)_{10-12}$ nanomolecules for high tumour specificity and cancer radiotherapy. *Adv. Mater.* **26**, 4565–4568 (2014).
5. Qin, W., Lohrman, J. & Ren, S. Q. Magnetic and optoelectronic properties of gold nanocluster-thiophene assembly. *Angew. Chem. Int. Ed.* **53**, 7316–7319 (2014).
6. Hembury, M. et al. Gold-silica quantum rattles for multimodal imaging and therapy. *Proc. Natl Acad. Sci. USA* **112**, 1959–1964 (2015).
7. Xue, S. H. et al. Protein MRI contrast agent with unprecedented metal selectivity and sensitivity for liver cancer imaging. *Proc. Natl Acad. Sci. USA* **112**, 6607–6612 (2015).
8. Vishnu, P. & Roy, V. Safety and efficacy of nab-paclitaxel in the treatment of patients with breast cancer. *Breast Cancer* **5**, 53–65 (2011).
9. Zhao, M. Z. et al. Quantitative proteomic analysis of cellular resistance to the nanoparticle abraxane. *ACS Nano* **9**, 10099–10112 (2015).
10. Cullis, J. et al. Macropinocytosis of nab-paclitaxel drives macrophage activation in pancreatic cancer. *Cancer Immunol. Res.* **5**, 182–190 (2017).
11. Svensson, M., Hakansson, A., Mossberg, A. K., Linse, S. & Svanborg, C. Conversion of α-lactalbumin to a protein inducing apoptosis. *Proc. Natl Acad. Sci. USA* **97**, 4221–4226 (2000).
12. Murakami, K., Andree, P. J. & Berliner, L. J. Metal ion binding to α-lactalbumin species. *Biochemistry* **21**, 5488–5494 (1982).

13. Nitta, K. & Sugai, S. The evolution of lysozyme and α-lactalbumin. *Eur. J. Biochem.* **182**, 111–118 (1989).
14. Wei, H. et al. Time-dependent, protein-directed growth of gold nanoparticles within a single crystal of lysozyme. *Nat. Nanotechnol.* **6**, 93–97 (2011).
15. Davis, A. M., Harris, B. J., Lien, E. L., Pramuk, K. & Trabulsi, J. α-Lactalbumin-rich infant formula fed to healthy term infants in a multicenter study: plasma essential amino acids and gastrointestinal tolerance. *Eur. J. Clin. Nutr.* **62**, 1294–1301 (2008).
16. Amitay, E. L. & Keinan-Boker, L. Breastfeeding and childhood leukemia incidence: a meta-analysis and systematic review. *JAMA Pediatr.* **169**, e151025 (2015).
17. Collaborative Group on Hormonal Factors in Breast Cancer. Breast cancer and breastfeeding: collaborative reanalysis of individual data from 47 epidemiological studies in 30 countries, including 50302 women with breast cancer and 96973 women without the disease. *Lancet* **360**, 187–195 (2002).
18. Jaini, R. et al. An autoimmune-mediated strategy for prophylactic breast cancer vaccination. *Nat. Med.* **16**, 799–803 (2010).
19. Mossberg, A. K. et al. Bladder cancers respond to intravesical instillation of HAMLET (human α-lactalbumin made lethal to tumour cells). *Int. J. Cancer* **121**, 1352–1359 (2007).
20. Gustafsson, L., Leijonhufvud, I., Aronsson, A., Mossberg, A. & Svanborg, C. Treatment of skin papillomas with topical α-lactalbumin-oleic acid. *N. Engl. J. Med.* **350**, 2663–2672 (2004).
21. Rosen, L. S., Ashurst, H. L. & Chap, L. Targeting signal transduction pathways in metastatic breast cancer: a comprehensive review. *Oncologist* **15**, 216–235 (2010).
22. Wang, Q. et al. Low toxicity and long circulation time of polyampholyte-coated magnetic nanoparticles for blood pool contrast agents. *Sci. Rep.* **5**, 7774 (2015).
23. Wu, Z. K. & Jin, R. C. On the ligand's role in the fluorescence of gold nanoclusters. *Nano Lett.* **10**, 2568–2573 (2010).
24. Duconseille, A., Astruc, T., Quintana, N., Meersman, F. & Sante-Lhoutellier, V. Gelatin structure and composition linked to hard capsule dissolution: a review. *Food Hydrocoll.* **43**, 360–376 (2015).
25. Poole, L. B. The basics of thiols and cysteines in redox biology and chemistry. *Free Radic. Biol. Med.* **80**, 148–157 (2015).
26. Chaudhuri, A. et al. Protein-dependent membrane interaction of a partially disordered protein complex with oleic acid: implications for cancer lipidomics. *Sci. Rep.* **6**, 35015 (2016).
27. Svensson, M. et al. α-Lactalbumin unfolding is not sufficient to cause apoptosis, but is required for the conversion to HAMLET (human alpha-lactalbumin made lethal to tumour cells). *Protein Sci.* **12**, 2794–2804 (2003).
28. Schmidbaur, H. The aurophilicity phenomenon: a decade of experimental findings, theoretical concepts and emerging applications. *Gold Bull.* **33**, 3–10 (2000).
29. Huang, K. Y. et al. Size-dependent localization and penetration of ultrasmall gold nanoparticles in cancer cells, multicellular spheroids, and tumours in vivo. *ACS Nano* **6**, 4483–4493 (2012).
30. Ha, K. D., Bidlingmaier, S. M. & Liu, B. Macropinocytosis exploitation by cancers and cancer therapeutics. *Front. Physiol.* **7**, 381 (2016).
31. Palm, W. et al. The utilization of extracellular proteins as nutrients is suppressed by mTORC1. *Cell* **162**, 259–270 (2015).
32. Ali, S. et al. Increased Ras GTPase activity is regulated by miRNAs that can be attenuated by CDF treatment in pancreatic cancer cells. *Cancer Lett.* **319**, 173–181 (2012).
33. Salloum, D., Mukhopadhyay, S., Tung, K., Polonetskaya, A. & Foster, D. A. Mutant ras elevates dependence on serum lipids and creates a synthetic lethality for rapamycin. *Mol. Cancer Ther.* **13**, 733–741 (2014).
34. Huang, J. L. et al. Lipoprotein-biomimetic nanostructure enables efficient targeting delivery of siRNA to Ras-activated glioblastoma cells via macropinocytosis. *Nat. Commun.* **8**, 15144 (2017).
35. Kerr, M. C. et al. Visualisation of macropinosome maturation by the recruitment of sorting nexins. *J. Cell Sci.* **119**, 3967–3980 (2006).
36. Cheng, Z. et al. Near-infrared fluorescent deoxyglucose analogue for tumour optical imaging in cell culture and living mice. *Bioconjug. Chem.* **17**, 662–669 (2006).
37. Grover-McKay, M., Walsh, S. A., Seftor, E. A., Thomas, P. A. & Hendrix, M. J. Role for glucose transporter 1 protein in human breast cancer. *Pathol. Oncol. Res.* **4**, 115–120 (1998).
38. Whittle, J. R., Lewis, M. T., Lindeman, G. J. & Visvader, J. E. Patient-derived xenograft models of breast cancer and their predictive power. *Breast Cancer Res.* **17**, 17 (2015).
39. Savci-Heijink, C. D. et al. Retrospective analysis of metastatic behaviour of breast cancer subtypes. *Breast Cancer Res. Treat.* **150**, 547–557 (2015).
40. Hu, W. et al. Protein corona-mediated mitigation of cytotoxicity of graphene oxide. *ACS Nano* **5**, 3693–3700 (2011).
41. Schneditz, D., Haditsch, B., Jantscher, A., Ribitsch, W. & Krisper, P. Absolute blood volume and hepatosplanchnic blood flow measured by indocyanine green kinetics during hemodialysis. *ASAIO J.* **60**, 452–458 (2014).
42. Ruggiero, A. et al. Paradoxical glomerular filtration of carbon nanotubes. *Proc. Natl Acad. Sci. USA* **107**, 12369–12374 (2010).
43. Choi, H. S. et al. Renal clearance of quantum dots. *Nat. Biotechnol.* **25**, 1165–1170 (2007).
44. Kamijima, T. et al. Heat-treatment method for producing fatty acid-bound α-lactalbumin that induces tumour cell death. *Biochem. Biophys. Res. Commun.* **376**, 211–214 (2008).
45. Rath, E. M., Duff, A. P., Hakansson, A. P., Knott, R. B. & Church, W. B. Small-angle X-ray scattering of BAMLET at pH 12: a complex of α-lactalbumin and oleic acid. *Proteins* **82**, 1400–1408 (2014).
46. Liu, D., Zhou, P., Liu, X. & Labuza, T. P. Moisture-induced aggregation of alpha-lactalbumin: effects of temperature, cations, and pH. *J. Food Sci.* **76**, C817–C823 (2011).
47. Permyakov, S. E. et al. A novel method for preparation of HAMLET-like protein complexes. *Biochimie* **93**, 1495–1501 (2011).
48. Balvan, J. et al. Multimodal holographic microscopy: distinction between apoptosis and oncosis. *PLoS ONE* **10**, e0121674 (2015).
49. Storm, P. et al. Conserved features of cancer cells define their sensitivity to HAMLET-induced death; c-Myc and glycolysis. *Oncogene* **30**, 4765–4779 (2011).
50. Ho, J. C. S., Nadeem, A., Rydstrom, A., Puthia, M. & Svanborg, C. Targeting of nucleotide-binding proteins by HAMLET—a conserved tumour cell death mechanism. *Oncogene* **35**, 897–907 (2016).
51. Chu, I. M. et al. Expression of GATA3 in MDA-MB-231 triple-negative breast cancer cells induces a growth inhibitory response to TGFβ. *PLoS ONE* **8**, e61125 (2013).
52. Deckers, M. et al. The tumour suppressor Smad4 is required for transforming growth factor beta-induced epithelial to mesenchymal transition and bone metastasis of breast cancer cells. *Cancer Res.* **66**, 2202–2209 (2006).
53. Morrow, K. A. et al. Loss of tumour suppressor Merlin in advanced breast cancer is due to post-translational regulation. *J. Biol. Chem.* **286**, 40376–40385 (2011).
54. Bockbrader, K. M., Tan, M. & Sun, Y. A small molecule Smac-mimic compound induces apoptosis and sensitizes TRAIL- and etoposide-induced apoptosis in breast cancer cells. *Oncogene* **24**, 7381–7388 (2005).
55. Hodgson, M. C. et al. INPP4B suppresses prostate cancer cell invasion. *Cell Commun. Signal.* **12**, 61 (2014).
56. Zhang, X. et al. Notch3 inhibits epithelial-mesenchymal transition by activating Kibra-mediated Hippo/YAP signaling in breast cancer epithelial cells. *Oncogenesis* **5**, e269 (2016).
57. Bhat, A. A. et al. Claudin-7 expression induces mesenchymal to epithelial transformation (MET) to inhibit colon tumourigenesis. *Oncogene* **34**, 4570–4580 (2015).
58. Garg, R. et al. Protein kinase C and cancer: what we know and what we do not. *Oncogene* **33**, 5225–5237 (2014).
59. Plotkin, L. I., Manolagas, S. C. & Bellido, T. Transduction of cell survival signals by connexin-43 hemichannels. *J. Biol. Chem.* **277**, 8648–8657 (2002).
60. Li, S. et al. Translation factor eIF4E rescues cells from Myc-dependent apoptosis by inhibiting cytochrome *c* release. *J. Biol. Chem.* **278**, 3015–3022 (2003).
61. Ríos, M. et al. AMPK activation by oncogenesis is required to maintain cancer cell proliferation in astrocytic tumors. *Cancer Res.* **73**, 2628–2638 (2013).
62. Liang, J. et al. Mitochondrial PKM2 regulates oxidative stress-induced apoptosis by stabilizing Bcl2. *Cell Res.* **27**, 329–351 (2017).
63. Walsh, L. A. et al. An integrated systems biology approach identifies TRIM25 as a key determinant of breast cancer metastasis. *Cell Rep.* **20**, 1623–1640 (2017).
64. Tekedereli, I. et al. Targeted silencing of elongation factor 2 kinase suppresses growth and sensitizes tumours to doxorubicin in an orthotopic model of breast cancer. *PLoS ONE* **7**, e41171 (2012).
65. Ahmed, S. U. & Milner, J. Basal cancer cell survival involves JNK2 suppression of a novel JNK1/c-Jun/Bcl-3 apoptotic network. *PLoS ONE* **4**, e7305 (2009).
66. Song, Q. et al. YAP enhances autophagic flux to promote breast cancer cell survival in response to nutrient deprivation. *PLoS ONE* **10**, e0120790 (2015).
67. Smith, G. C., d'Adda di Fagagna, F., Lakin, N. D. & Jackson, S. P. Cleavage and inactivation of ATM during apoptosis. *Mol. Cell. Biol.* **19**, 6076–6084 (1999).
68. Fu, K. et al. DJ-1 inhibits TRAIL-induced apoptosis by blocking pro-caspase-8 recruitment to FADD. *Oncogene* **31**, 1311–1322 (2012).
69. Yellen, P. et al. High-dose rapamycin induces apoptosis in human cancer cells by dissociating mTOR complex 1 and suppressing phosphorylation of 4E-BP1. *Cell Cycle* **10**, 3948–3956 (2011).
70. Masters, S. C. & Fu, H. 14-3-3 proteins mediate an essential anti-apoptotic signal. *J. Biol. Chem.* **276**, 45193–45200 (2001).
71. Chen, L. et al. Inhibition of the p38 kinase suppresses the proliferation of human ER-negative breast cancer cells. *Cancer Res.* **69**, 8853–8861 (2009).

72. Tafolla, E., Wang, S., Wong, B., Leong, J. & Kapila, Y. L. JNK1 and JNK2 oppositely regulate p53 in signaling linked to apoptosis triggered by an altered fibronectin matrix: JNK links FAK and p53. *J. Biol. Chem.* **280**, 19992–19999 (2005).
73. Yamamoto, Y. & Gaynor, R. B. Therapeutic potential of inhibition of the NF-κB pathway in the treatment of inflammation and cancer. *J. Clin. Invest.* **107**, 135–142 (2001).
74. Naidu, S., Wijayanti, N., Santoso, S., Kietzmann, T. & Immenschuh, S. An atypical NF-κB-regulated pathway mediates phorbol ester-dependent heme oxygenase-1 gene activation in monocytes. *J. Immunol.* **181**, 4113–4123 (2008).
75. Russo, P., Arzani, D., Trombino, S. & Falugi, C. *c-myc* down-regulation induces apoptosis in human cancer cell lines exposed to RPR-115135 ($C_{31}H_{29}NO_4$), a non-peptidomimetic farnesyltransferase inhibitor. *J. Pharmacol. Exp. Ther.* **304**, 37–47 (2003).
76. Le Mellay, V., Troppmair, J., Benz, R. & Rapp, U. R. Negative regulation of mitochondrial VDAC channels by C-Raf kinase. *BMC Cell Biol.* **3**, 14 (2002).
77. Obeid, M. et al. Calreticulin exposure dictates the immunogenicity of cancer cell death. *Nat. Med.* **13**, 54–61 (2007).
78. Wong, C. W., Seow, H. F., Husband, A. J., Regester, G. O. & Watson, D. L. Effects of purified bovine whey factors on cellular immune functions in ruminants. *Vet. Immunol. Immunopathol.* **56**, 85–96 (1997).
79. Kim, S. E. et al. Ultrasmall nanoparticles induce ferroptosis in nutrient-deprived cancer cells and suppress tumour growth. *Nat. Nanotechnol.* **11**, 977–985 (2016).
80. Ohkuri, T. et al. A protein's conformational stability is an immunologically dominant factor: evidence that free-energy barriers for protein unfolding limit the immunogenicity of foreign proteins. *J. Immunol.* **185**, 4199–4205 (2010).
81. Xie, J., Zheng, Y. & Ying, J. Y. Protein-directed synthesis of highly fluorescent gold nanoclusters. *J. Am. Chem. Soc.* **131**, 888–889 (2009).
82. Pfeil, W. Is thermally denatured protein unfolded? The example of alpha-lactalbumin. *Biochim. Biophys. Acta* **911**, 114–116 (1987).
83. Duff, D. G., Baiker, A. & Edwards, P. P. A new hydrosol of gold clusters. 1. Formation and particle size variation. *Langmuir* **9**, 2301–2309 (1993).
84. Micsonai, A. et al. Accurate secondary structure prediction and fold recognition for circular dichroism spectroscopy. *Proc. Natl Acad. Sci. USA* **112**, E3095–E3103 (2015).
85. Eaton, D. F. International union of pure and applied chemistry organic chemistry division commission on photochemistry. Reference materials for fluorescence measurement. *J. Photochem. Photobiol. B* **2**, 523–531 (1988).
86. Marques, M. R. C., Loebenberg, R. & Almukainzi, M. Simulated biological fluids with possible application in dissolution testing. *Dissolut. Technol.* **18**, 15–28 (2011).
87. Liskova, K., Kelly, A. L., O'Brien, N. & Brodkorb, A. Effect of denaturation of α-lactalbumin on the formation of BAMLET (bovine α-lactalbumin made lethal to tumour cells). *J. Agric. Food Chem.* **58**, 4421–4427 (2010).
88. Wawrik, B. & Harriman, B. H. Rapid, colourimetric quantification of lipid from algal cultures. *J. Microbiol. Methods* **80**, 262–266 (2010).
89. Ashburner, M. et al. Gene ontology: tool for the unification of biology. *Nat. Genet.* **25**, 25–29 (2000).
90. UniProt Consortium. UniProt: a hub for protein information. *Nucleic Acids Res.* **43**, D204–D212 (2015).
91. Martijn, T & Ellis, P. Treemap: treemap visualization. Treemap v2.4-2 (Martijn, T., 2017); https://cran.r-project.org/web/packages/treemap/index.html
92. Martin, M., Seth, F. & Robert, G. GSEABase: gene set enrichment data structures and methods. GSEABase v1.5 (Bioconductor Package Maintainer, 2016); https://bioconductor.org/packages/release/bioc/html/GSEABase.html
93. Gentleman, R. C. et al. Bioconductor: open software development for computational biology and bioinformatics. *Genome Biol.* **5**, R80 (2004).
94. Nioka, S. et al. Simulation study of breast tissue hemodynamics during pressure perturbation. *Adv. Exp. Med. Biol.* **566**, 17–22 (2005).

Acknowledgements

We thank Agropur Ingredients for providing the high-purity bovine α-LA samples used in the study. We acknowledge the staff at the following core facilities at Memorial Sloan Kettering Cancer Center (MSKCC): the Molecular Cytology Core, Small Animal Imaging Core Facility, Electron Microscopy Core, Flow Cytometry Core, NMR Analytical Core and Microchemistry and Proteomics Core. We also thank C. LeKaye and D. Winkleman at the MSKCC MRI core facilities, C.-G. Lee and J. Jimenez of the CLC Imaging Core at Weill Cornell Medical College, C. Adura at the High Throughput and Spectroscopy Resource Center of Rockefeller University for their technical support; current and former Kircher lab members for helpful discussions and critical reading of the manuscript; staff at the Functional Proteomics RPPA Core facility at MD Anderson Cancer Center and M. Wlodarczyk from Brooklyn College at the City University of New York for carrying out atomic absorption spectroscopy; and W. Zhang from the University of Wisconsin-Madison for helping with the schematic figures. The following funding sources to M.F.K. are acknowledged: NIH (nos. R01 EB017748, R01 CA222836 and K08 CA16396); Dana-Farber Innovations Research Fund (IRF); Parker Institute for Cancer Immunotherapy; Pershing Square Sohn Prize by the Pershing Square Sohn Cancer Research Alliance. M.F.K. is a Damon Runyon-Rachleff Innovator who was supported (in part) by the Damon Runyon Cancer Research Foundation (no. DRR-29-14), and the Mr. William H. and Mrs. Alice Goodwin and the Commonwealth Foundation for Cancer Research and the Experimental Therapeutics Center of MSKCC. We also acknowledge the grant-funding support provided by the MSKCC NIH Core Grant (no. P30-CA008748) and NIH Prostate SPORE (no. P50-CA92629). G.C. is supported by the NIH (nos. R01 CA172546, P01 CA186866 and P50 CA86438) and the Mr. William H. and Mrs. Alice Goodwin and the Commonwealth Foundation for Cancer Research and the Experimental Therapeutics Center of MSKCC. T.W. is supported by the Lymphoma Research Foundation. The Functional Proteomics RPPA Core at MD Anderson Cancer Center is supported a NIH Support Grant (no. P30 CA016672-40).The National Natural Science Foundation of China (no. 31971311) to L.Z. are also acknowledged. .

Author contributions

J.Y. and M.F.K. conceived and designed the experiments and co-wrote the manuscript. J.Y. synthesized and characterized AuQCs. Schematic atomic structures of AuQCs were provided by L.Z. Animal studies were performed by J.Y., V.K.R., H.H., H.Z., R.H. and J.H.H. MALDI was performed by R.C.H. and M.M.M. Pathway analysis was conducted by T.W. and G.C., and biochemical studies were run by S.J.; M.B.B. took AFM images and HPLC was performed by W.P.; J.Y., T.W., S.J., C.A., S.P., I.J.C., J.H.H., G.C. and M.F.K. analysed data. The project was supervised by M.F.K. and the manuscript was reviewed and approved by all of the authors.

Competing interests

J.Y. and M.F.K. have filed a pending patent application related to this work.

Additional information

Supplementary information is available for this paper at https://doi.org/10.1038/s41551-020-0584-z.

Correspondence and requests for materials should be addressed to M.F.K.

Reprints and permissions information is available at www.nature.com/reprints.

Publisher's note Springer Nature remains neutral with regard to jurisdictional claims in published maps and institutional affiliations.

nature research

Corresponding author(s): Moritz F. Kircher

Last updated by author(s): Jun 9, 2020

Reporting Summary

Nature Research wishes to improve the reproducibility of the work that we publish. This form provides structure for consistency and transparency in reporting. For further information on Nature Research policies, see our Editorial Policies and the Editorial Policy Checklist.

Statistics

For all statistical analyses, confirm that the following items are present in the figure legend, table legend, main text, or Methods section.

n/a	Confirmed	
☐	☒	The exact sample size (*n*) for each experimental group/condition, given as a discrete number and unit of measurement
☐	☒	A statement on whether measurements were taken from distinct samples or whether the same sample was measured repeatedly
☐	☒	The statistical test(s) used AND whether they are one- or two-sided *Only common tests should be described solely by name; describe more complex techniques in the Methods section.*
☒	☐	A description of all covariates tested
☒	☐	A description of any assumptions or corrections, such as tests of normality and adjustment for multiple comparisons
☐	☒	A full description of the statistical parameters including central tendency (e.g. means) or other basic estimates (e.g. regression coefficient) AND variation (e.g. standard deviation) or associated estimates of uncertainty (e.g. confidence intervals)
☐	☒	For null hypothesis testing, the test statistic (e.g. *F*, *t*, *r*) with confidence intervals, effect sizes, degrees of freedom and *P* value noted *Give P values as exact values whenever suitable.*
☒	☐	For Bayesian analysis, information on the choice of priors and Markov chain Monte Carlo settings
☒	☐	For hierarchical and complex designs, identification of the appropriate level for tests and full reporting of outcomes
☒	☐	Estimates of effect sizes (e.g. Cohen's *d*, Pearson's *r*), indicating how they were calculated

Our web collection on statistics for biologists contains articles on many of the points above.

Software and code

Policy information about availability of computer code

Data collection	Living Image 4.5. BD FACSDiva. Zeiss Zen 2. SoftMax Pro 7. Leica Application Suite.
Data analysis	Origin Lab Pro 2020. Graphpad Prism 8. ImageJ. R. Living Image 4.5. FlowJo V10. Bitplane Imaris 9. Zeiss Zen 2. Pannoramic Viewer 1.15. UCSF Chimera 1.11. Microsoft Excel 2016, Customized R codes (available at https://github.com/wangtaifr/Kircher2020).

For manuscripts utilizing custom algorithms or software that are central to the research but not yet described in published literature, software must be made available to editors and reviewers. We strongly encourage code deposition in a community repository (e.g. GitHub). See the Nature Research guidelines for submitting code & software for further information.

Data

Policy information about availability of data

All manuscripts must include a data availability statement. This statement should provide the following information, where applicable:

- Accession codes, unique identifiers, or web links for publicly available datasets
- A list of figures that have associated raw data
- A description of any restrictions on data availability

The main data supporting the results in this study are available within the paper and its Supplementary Information. The raw and analysed datasets generated during the study are too large to be publicly shared, yet they are available for research purposes from the corresponding authors on reasonable request.

Field-specific reporting

Please select the one below that is the best fit for your research. If you are not sure, read the appropriate sections before making your selection.

☒ Life sciences ☐ Behavioural & social sciences ☐ Ecological, evolutionary & environmental sciences

For a reference copy of the document with all sections, see nature.com/documents/nr-reporting-summary-flat.pdf

Life sciences study design

All studies must disclose on these points even when the disclosure is negative.

Sample size	No statistical method was applied to predetermine sample size. Sample sizes in the study were chosen to comply with local animal-ethics policies and financial constraints, to use the smallest possible number of animals to obtain data. They are all commensurate with traditions in the field.
Data exclusions	No data were excluded.
Replication	Experimental findings were reproduced. All attempts at replication were successful.
Randomization	Mice were randomly assigned into groups, grafted with tumors, allocated for treatments or used for toxicity, pharmacokinetic and biodistribution studies. No other randomizations were performed.
Blinding	No blinding was performed.

Reporting for specific materials, systems and methods

We require information from authors about some types of materials, experimental systems and methods used in many studies. Here, indicate whether each material, system or method listed is relevant to your study. If you are not sure if a list item applies to your research, read the appropriate section before selecting a response.

Materials & experimental systems

n/a	Involved in the study
☐	☒ Antibodies
☐	☒ Eukaryotic cell lines
☒	☐ Palaeontology and archaeology
☐	☒ Animals and other organisms
☒	☐ Human research participants
☒	☐ Clinical data
☒	☐ Dual use research of concern

Methods

n/a	Involved in the study
☒	☐ ChIP-seq
☐	☒ Flow cytometry
☒	☐ MRI-based neuroimaging

Antibodies

Antibodies used	anti-EEA1 (ab2900, Abcam, 0.8 µg/mL); anti-LAMP1 (1D4B, DSHB, 0.5 µg/mL); biotinylated goat anti-rabbit and goat anti-rat IgG (BA-1000 and BA-9401, Vector Labs,1:200 dilution); anti-Iba1 antibody (019-19741, Wako, 0.5 µg/mL); anti-β-actin (A1978, Sigma-Aldrich,1:5000 dilution); anti-p-Akt (Ser473)(9271, Cell Signaling, 1:1000 dilution); anti-Akt (9272, Cell Signaling, 1:500 dilution); anti-p-c-raf (Ser259)(9421, Cell Signaling, 1:1000 dilution); anti-p-MEK1/2(Ser217/221)(9154, Cell Signaling, 1:500 dilution);anti-p-ERK1/2(Thr202/Tyr204)(4370, Cell Signaling, 1:1000 dilution); anti-ERK1/2(9102, Cell Signaling, 1:1000 dilution); anti-c-myc (SC-764, Santa Cruz Biotechnologies, 1:500 dilution); anti-p-S6 (Ser235/236)(4858, Cell Signaling, 1:2000 dilution); anti-RIP1 Kinase (4926, Cell Signaling, 1:1000 dilution); anti-Bid (8762, Cell Signaling, 1:1000 dilution).
Validation	Antibodies were validated for western blot, immunofluorescence or immunohistochemistry.

Eukaryotic cell lines

Policy information about cell lines

Cell line source(s)	Cell lines in the study were acquired from the American Type Culture Collection (ATCC), including MDA-MB-231, BxPC-3, MDA-MB-468, 4T1, B16-F10 and LLC. MC-38 was acquired from the Cell Bank of the Chinese Academy of Sciences.
Authentication	No further authentication was performed.
Mycoplasma contamination	All cell lines used in the study tested negative of mycoplasma contamination.

Commonly misidentified lines (See ICLAC register)	No commonly misidentified cell lines were used.

Animals and other organisms

Policy information about studies involving animals; ARRIVE guidelines recommended for reporting animal research

Laboratory animals	All mice used in the study were female and acquired from the Jackson Laboratory (JAX). J:NU (Foxn1nu/Foxn1nu), BALB/cJ and NSG (NOD.Cg-Prkdcscid Il2rgtm1Wjl/SzJ) mice were used. Mice undergoing experimental procedures were 8–16 weeks old, depending on tumor-growth rates, and weighed 0.020–0.025 kg.
Wild animals	The study did not involve wild animals.
Field-collected samples	The study did not involve samples collected from the field.
Ethics oversight	All animal procedures were approved by the Institutional Animal Care and Use Committees (IACUC) at Memorial Sloan Kettering Cancer Center, following NIH guidelines.

Note that full information on the approval of the study protocol must also be provided in the manuscript.

Flow Cytometry

Plots

Confirm that:

☒ The axis labels state the marker and fluorochrome used (e.g. CD4-FITC).

☒ The axis scales are clearly visible. Include numbers along axes only for bottom left plot of group (a 'group' is an analysis of identical markers).

☒ All plots are contour plots with outliers or pseudocolor plots.

☒ A numerical value for number of cells or percentage (with statistics) is provided.

Methodology

Sample preparation	For apoptosis and necrosis staining, harvested cells were resuspended in binding buffer. CF488-Annexin V and EthD-III were added, followed by incubation at room temperature for 15 min away from light on a rotator and analyzed by flow cytometry. For cell-cycle analysis, harvested cells were fixed in drop-wise added ice-old 70% ethanol for 4 hrs at 4°C. After further washes with PBS, cells were stained with PI/RNase staining buffer (BD PharmingenTM) at room temperature for 30 min and immediately analysed by flow cytometry. For JC-1 assay, JC-1 was freshly prepared by diluting 1:10 v/v in 37°C culture medium, added to each well at a volumetric ratio of 1:10 to medium and incubated at 37°C for 30 min. Cells were harvested, washed twice with PBS and resuspended in JC-1 assay buffer for flow-cytometric analysis. Please refer to Methods for further details.
Instrument	BD LSR II (BD Biosciences)
Software	BD FACSDiva was used for collection, and FlowJo V10 was used for analysis.
Cell population abundance	No cell sorting was performed.
Gating strategy	Cells were gated on FSC/SSC-area and width.

☐ Tick this box to confirm that a figure exemplifying the gating strategy is provided in the Supplementary Information.